Working Group I Contribution to the Intergovernmental Panel on Climate Change Fourth Assessment Report

Climate Change 2007: The Physical Science Basis

Technical Summary Figures

Coordinating Lead Authors: Susan Solomon (USA), Dahe Qin (China), Martin Manning (USA, New Zealand)

Lead Authors: Richard Alley (USA), Terje Berntsen (Norway), Nathaniel L. Bindoff (Australia), Zhenlin Chen (China), Amnat Chidthaisong (Thailand), Jonathan Gregory (UK), Gabriele Hegerl (USA, Germany), Martin Heimann (Germany, Switzerland), Bruce Hewitson (South Africa), Brian Hoskins (UK), Fortunat Joos (Switzerland), Jean Jouzel (France), Vladimir Kattsov (Russia), Ulrike Lohmann (Switzerland), Taroh Matsuno (Japan), Mario Molina (USA, Mexico), Neville Nicholls (Australia), Jonathan Overpeck (USA), Graciela Raga (Mexico, Argentina), Venkatachalam Ramaswamy (USA), Jiawen Ren (China), Matilde Rusticucci (Argentina), Richard Somerville (USA), Thomas F. Stocker (Switzerland), Ronald J. Stouffer (USA), Penny Whetton (Australia), Richard A. Wood (UK), David Wratt (New Zealand)

Contributing Authors: Julie Arblaster (USA, Australia), Guy Brasseur (USA, Germany), Jens Hesselbjerg Christensen (Denmark), Kenneth Denman (Canada), David Fahey (USA), Piers Forster (UK), James Haywood (UK), Eystein Jansen (Norway, Germany), Philip D. Jones (UK), Reto Knutti (Switzerland), Hervé Le Treut (France), Peter Lemke (Germany), Gerald Meehl (USA), David Randall (USA), Daíthí A. Stone (UK), Kevin E. Trenberth (USA), Jürgen Willebrand (Germany), Francis Zwiers (Canada)

Review Editors: Kansri Boonpragob (Thailand), Filippo Giorgi (Italy), Bubu Pateh Jallow (The Gambia)

Date of Draft: 27 October 2006

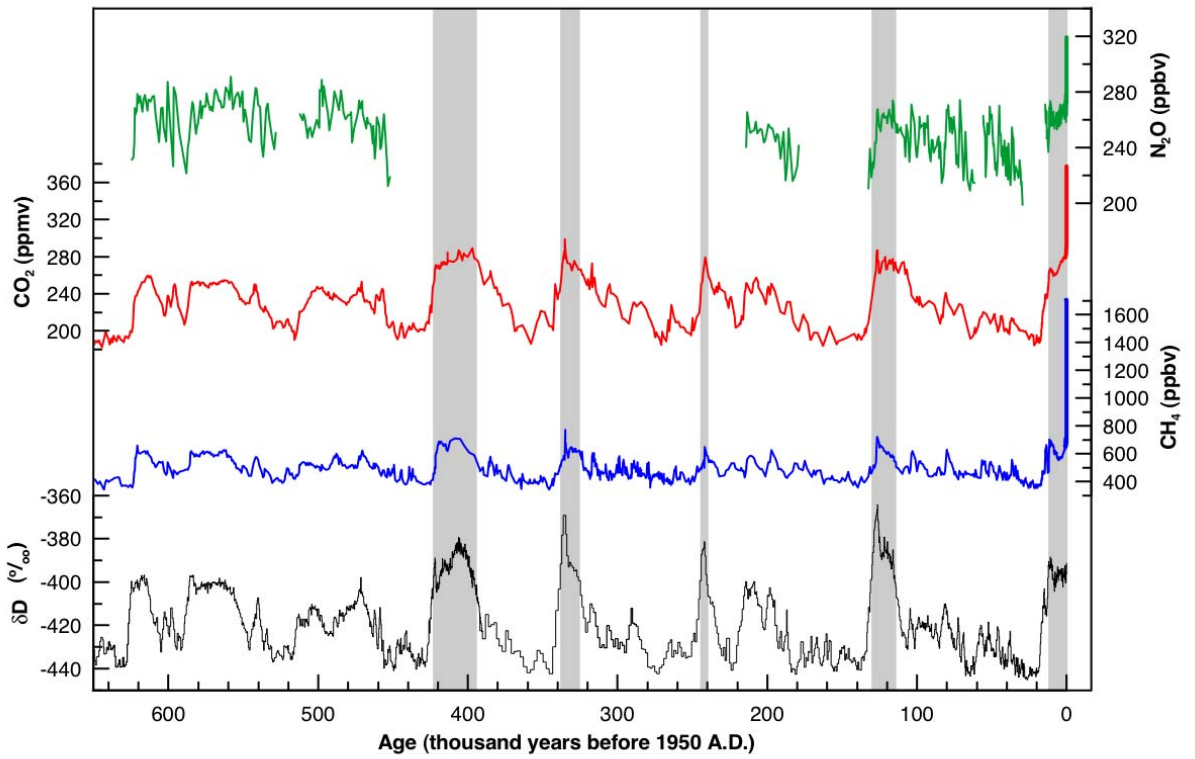

Figure TS-1. Variations of deuterium (δD) in Antarctic ice, which is a proxy for local temperature, and the atmospheric concentrations of the greenhouse gases carbon dioxide (CO_2), methane (CH_4), nitrous oxide (N_2O) in air trapped within these ice cores and from recent atmospheric measurements. Data cover 650,000 years and the shaded bands indicate previous interglacial warm periods. {Adapted from Figure 6.3}

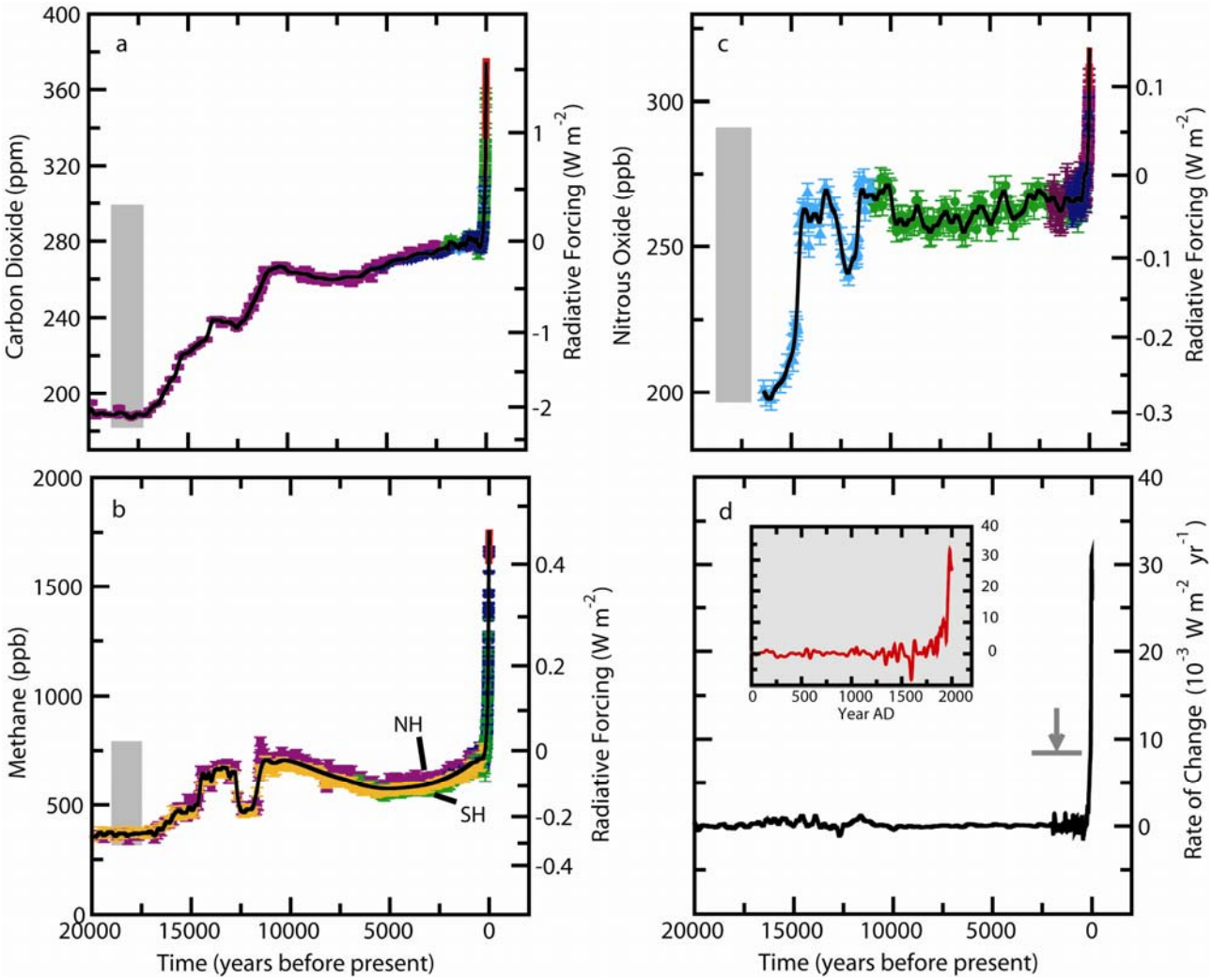

Figure TS-2. The concentrations and radiative forcing by (a) carbon dioxide (CO_2), (b) methane (CH_4), (c) nitrous oxide (N_2O), and (d) the rate of change in their combined radiative forcing over the last 20,000 years reconstructed from Antarctic and Greenland ice and firn data (symbols) and direct atmospheric measurements (red and magenta lines). The grey bars show the reconstructed ranges of natural variability for the past 650,000 years. The rate of change in radiative forcing (black line) has been computed from spline fits to the concentration data. The width of the age spread in the ice data varies from ~20 years for sites with a high accumulation of snow such as Law Dome, Antarctica, to ~200 years for low accumulation sites such as Dome C, Antarctica. The arrow shows the peak in the rate of change in radiative forcing that would result if the anthropogenic signals of CO_2, CH_4, and N_2O had been smoothed corresponding to conditions at the low accumulation Dome C site . The negative rate of change in forcing around 1600 AD shown in the higher resolution inset in panel d results from a CO_2 decrease of about 10 ppm in the Law Dome record. {Figure 6.4}

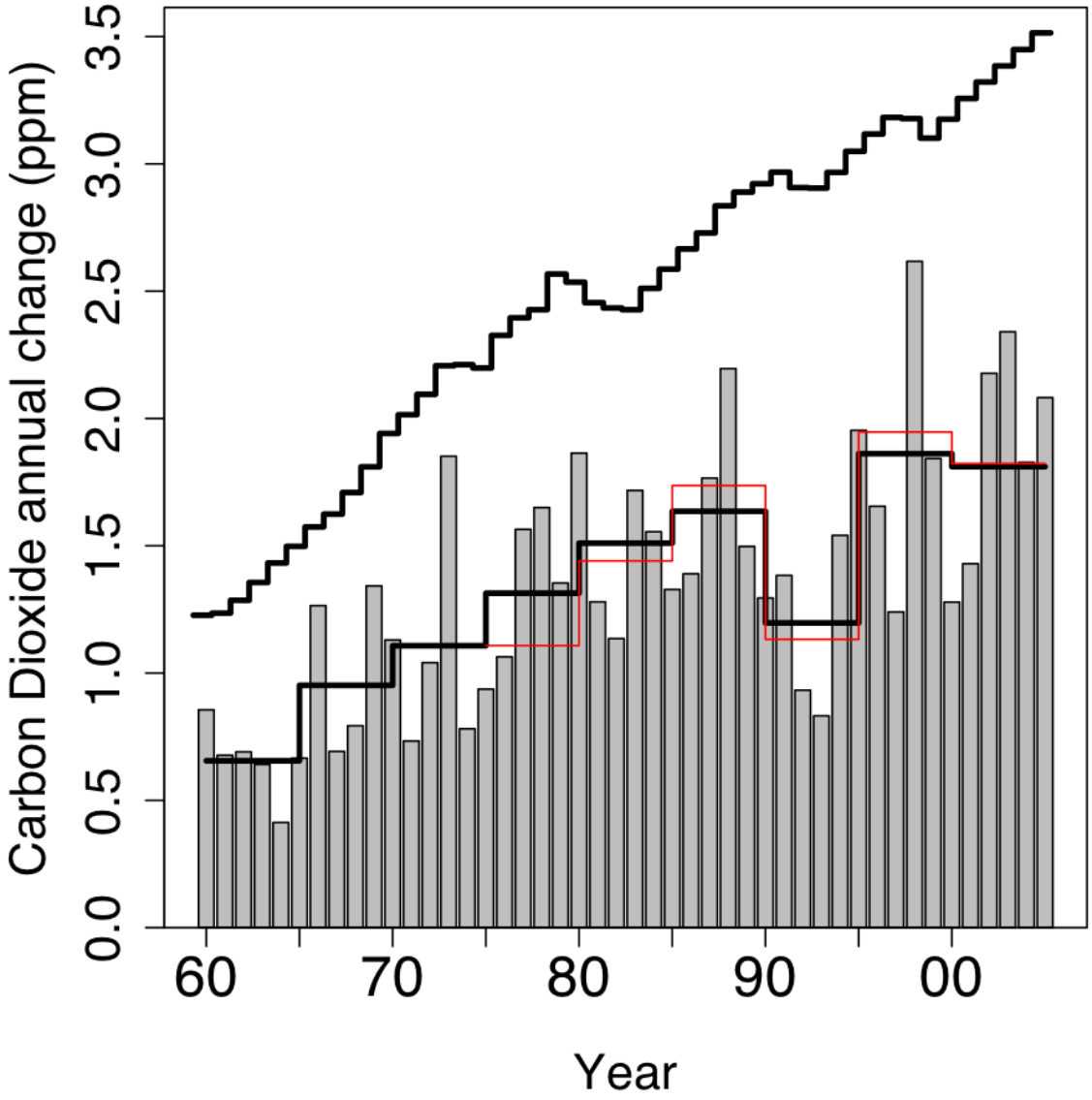

Figure TS-3. Annual changes in global mean CO_2 concentration (*grey bars*) and their 5-year means from two different measurement networks (*red and lower black stepped lines*). The 5-year means smooth out short term perturbations associated with strong ENSO events in 1972, 1982, 1987 and 1997. Uncertainties in the 5-year means are indicated by the difference between the red and lower black lines and are of order 0.15 ppm. The upper stepped line shows the annual increases that would occur if all fossil fuel emissions stayed in the atmosphere and there were no other emissions. Data sources are given in Chapter 7. {Figure 7.4}

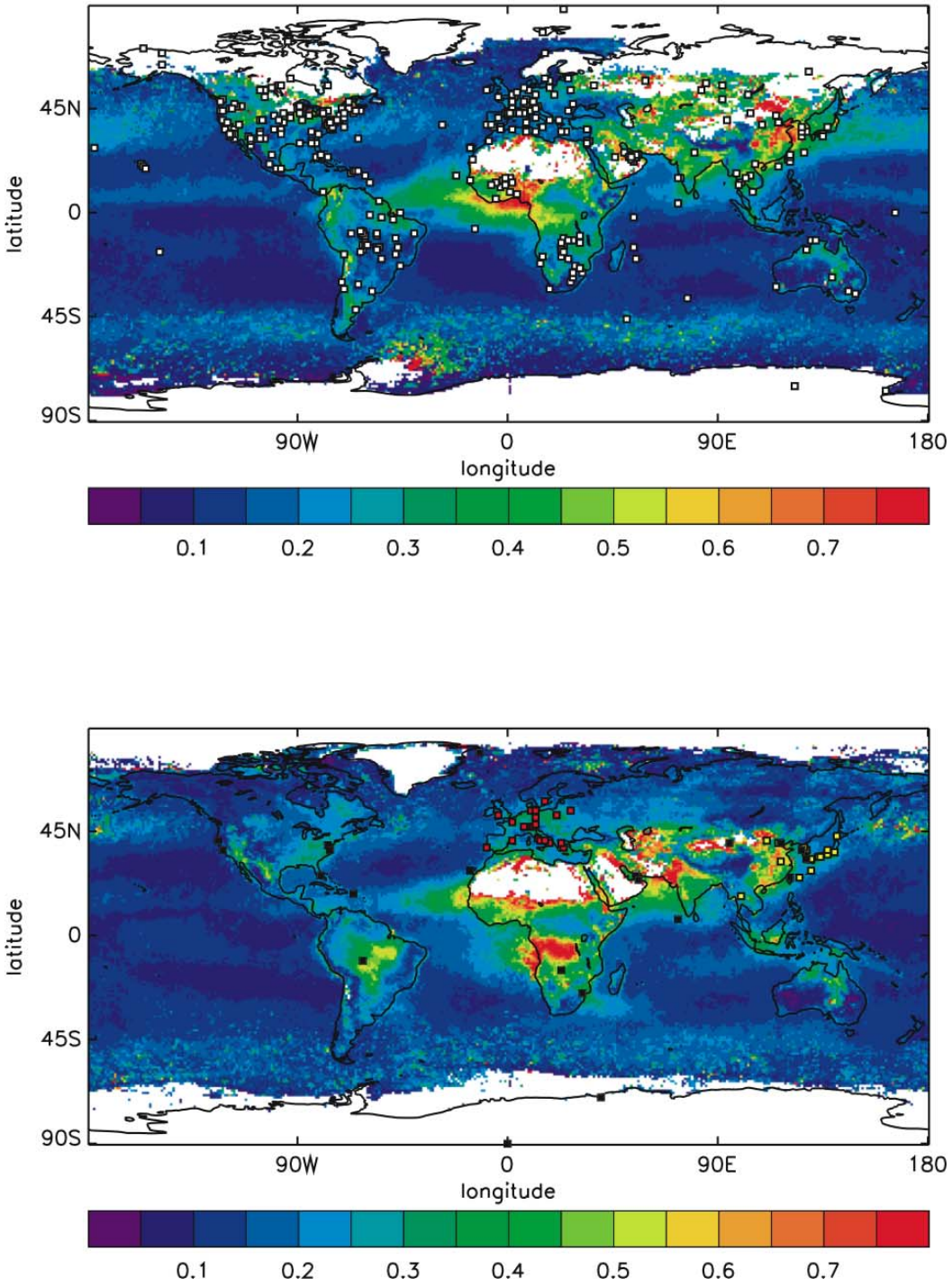

Figure TS-4. The total aerosol optical depth (due to natural plus anthropogenic aerosols) at a mid-visible wavelength determined by satellite measurements for January to March 2001 (top panel) and August to October 2001 (bottom panel), illustrating seasonal changes in industrial and biomass burning aerosols. Data come from satellite measurements complemented by two different kinds of ground based measurements at locations shown in the two panels (see Section 2.4.2 for details). {Figure 2.11}

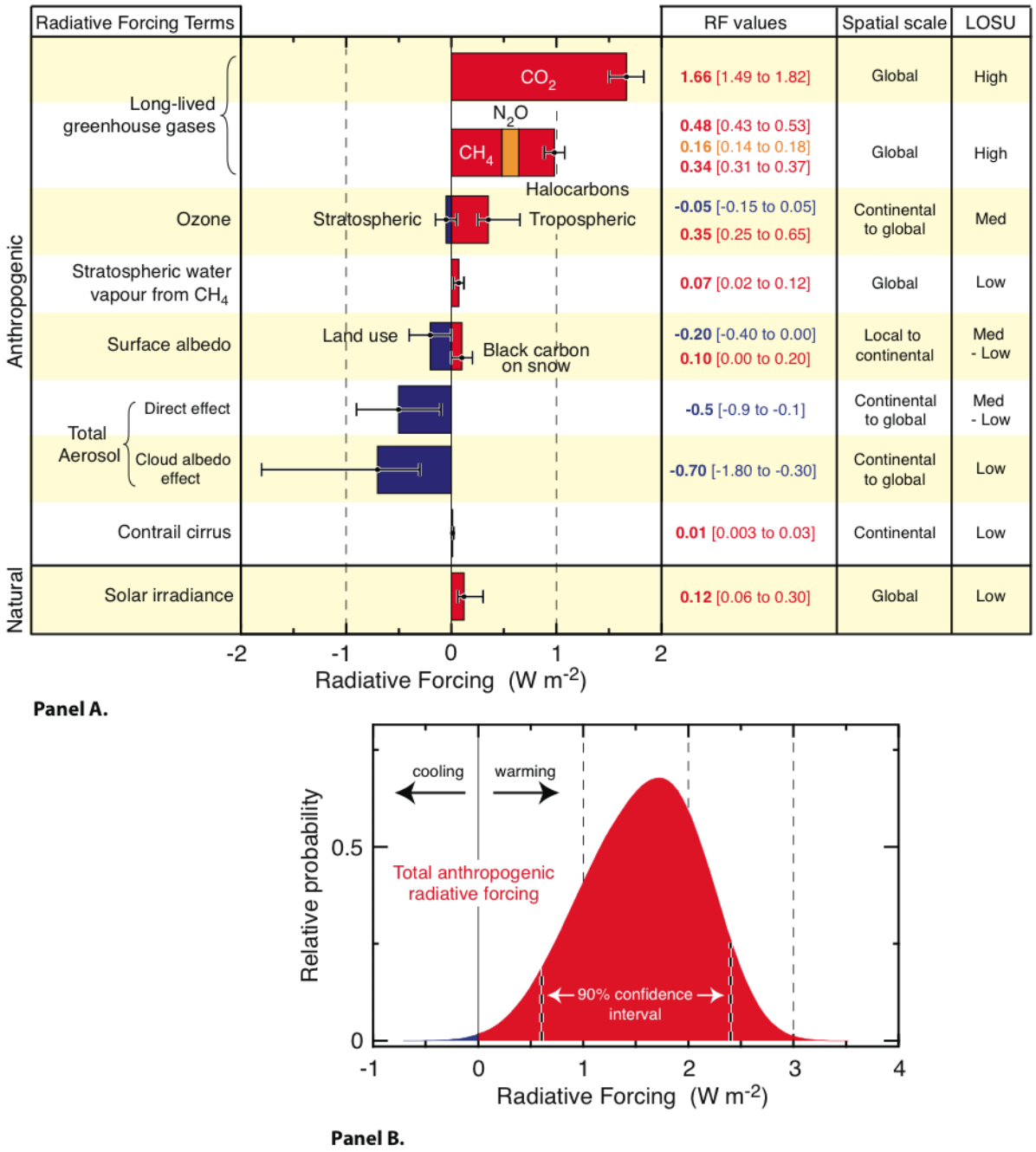

Figure TS-5. Global-mean radiative forcings (RF) and their 90% confidence intervals for various agents and mechanisms. Columns on the right hand side specify: (RF values) best estimates and confidence intervals; (Spatial scale) typical geographical extent of the forcing; (LOSU) Level of Scientific understanding indicating the scientific confidence level as explained in Section 2.9. Errors for CH_4, N_2O, and halocarbons have been combined. Volcanic aerosols contribute an additional form of natural forcing but can not be included due to their episodic nature. *Panel B*: Probability distribution of the global-mean combined radiative forcing from all anthropogenic agents shown in Panel A. The distribution is calculated by combining the best estimates and uncertainties of each component. The spread in the distribution is increased significantly by the negative forcing terms which have larger uncertainties than the positive terms. {Sections 2.9.1, 2.9.2; Figure 2.20}

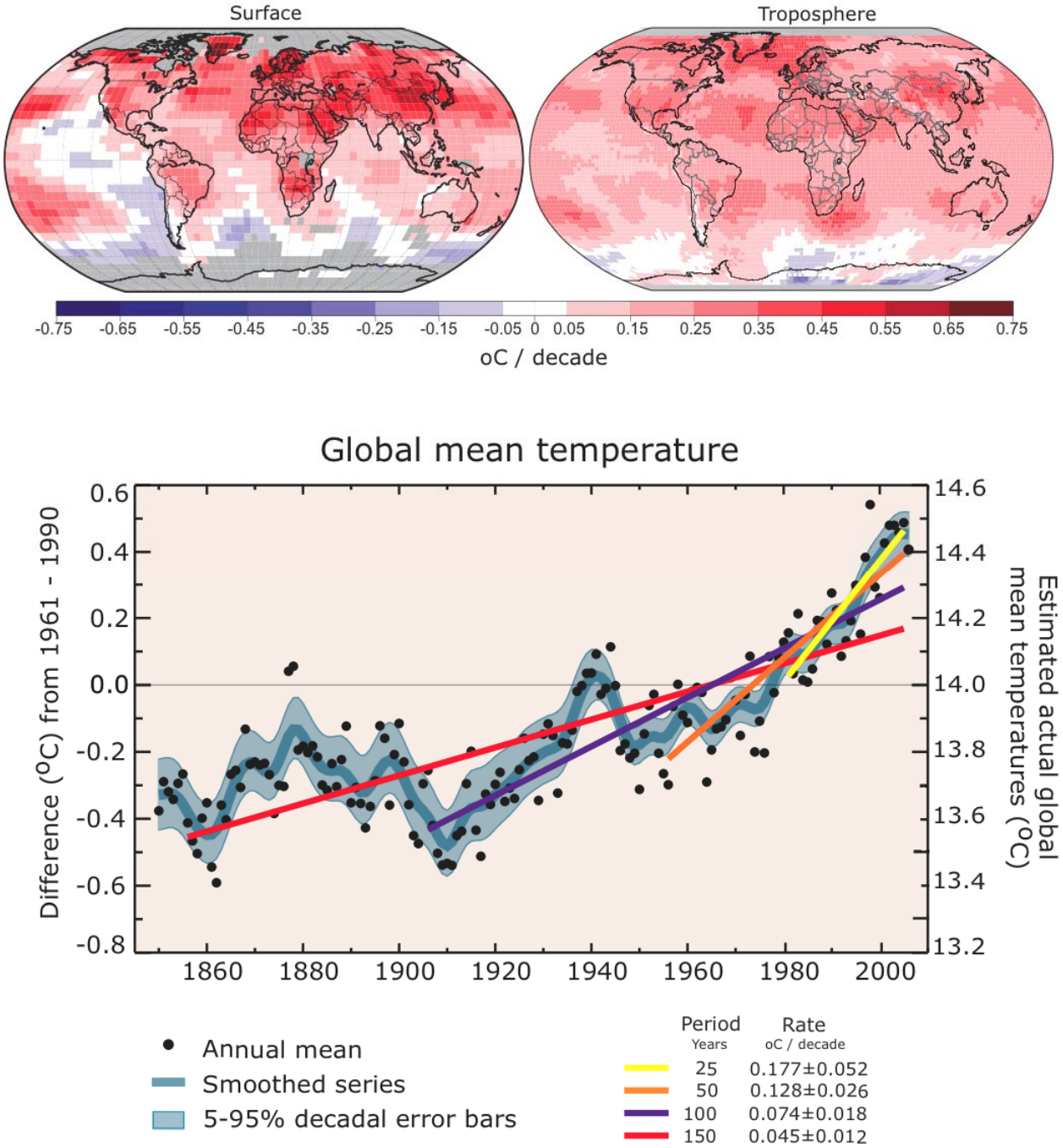

Figure TS-6. *Top*: Patterns of linear global temperature trends 1979 to 2005 estimated at the surface (left), and for the troposphere from satellite records (right). Grey indicates areas with incomplete data. *Bottom*: Annual global mean temperatures (black dots) with linear fits to the data. The left hand axis shows temperature anomalies relative to the 1961 to 1990 average and the right hand axis shows estimated actual temperatures, both in ºC. Linear trends are shown for the last 25 (yellow), 50 (orange), 100 (magenta) and 150 years (red). The blue line is a smoothed depiction to capture the decadal variations, with the decadal 90% error range shown as a pale blue band about that line. The temperature change from the first 70 years of the instrumental record (1850–1919) to the last 5 years (2001–2005) is 0.78 ± 0.18ºC. {FAQ 3.1, Figure 1.}

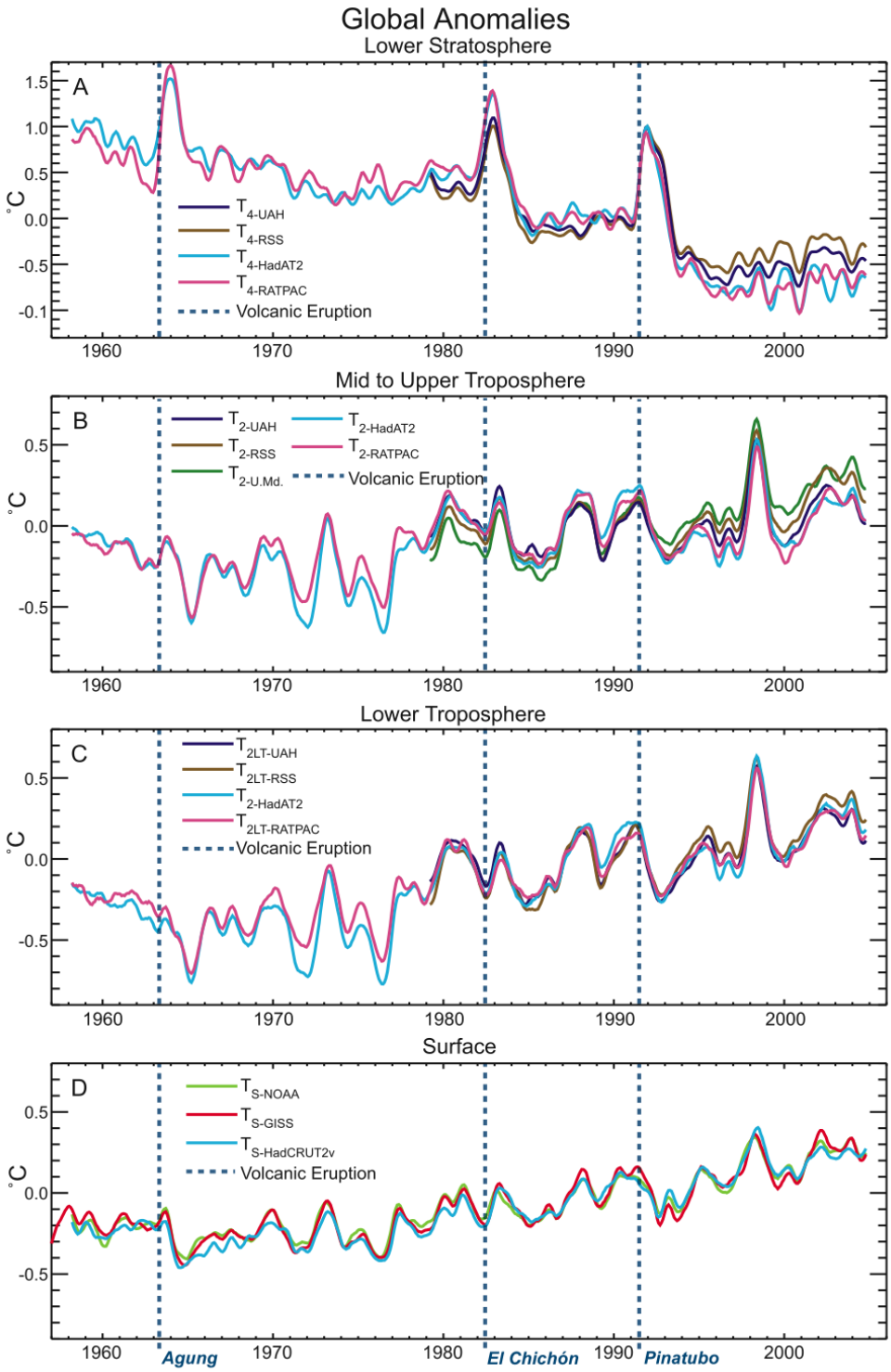

Figure TS-7. Observed surface (panel D) and upper air temperatures for the lower troposphere (panel C), mid to upper troposphere (panel B) and lower stratosphere (Panel A), as monthly mean anomalies relative to 1979–1997 smoothed with a 7-month running mean filter. Dashed lines indicate the times of major volcanic eruptions. {Figure 3.17}

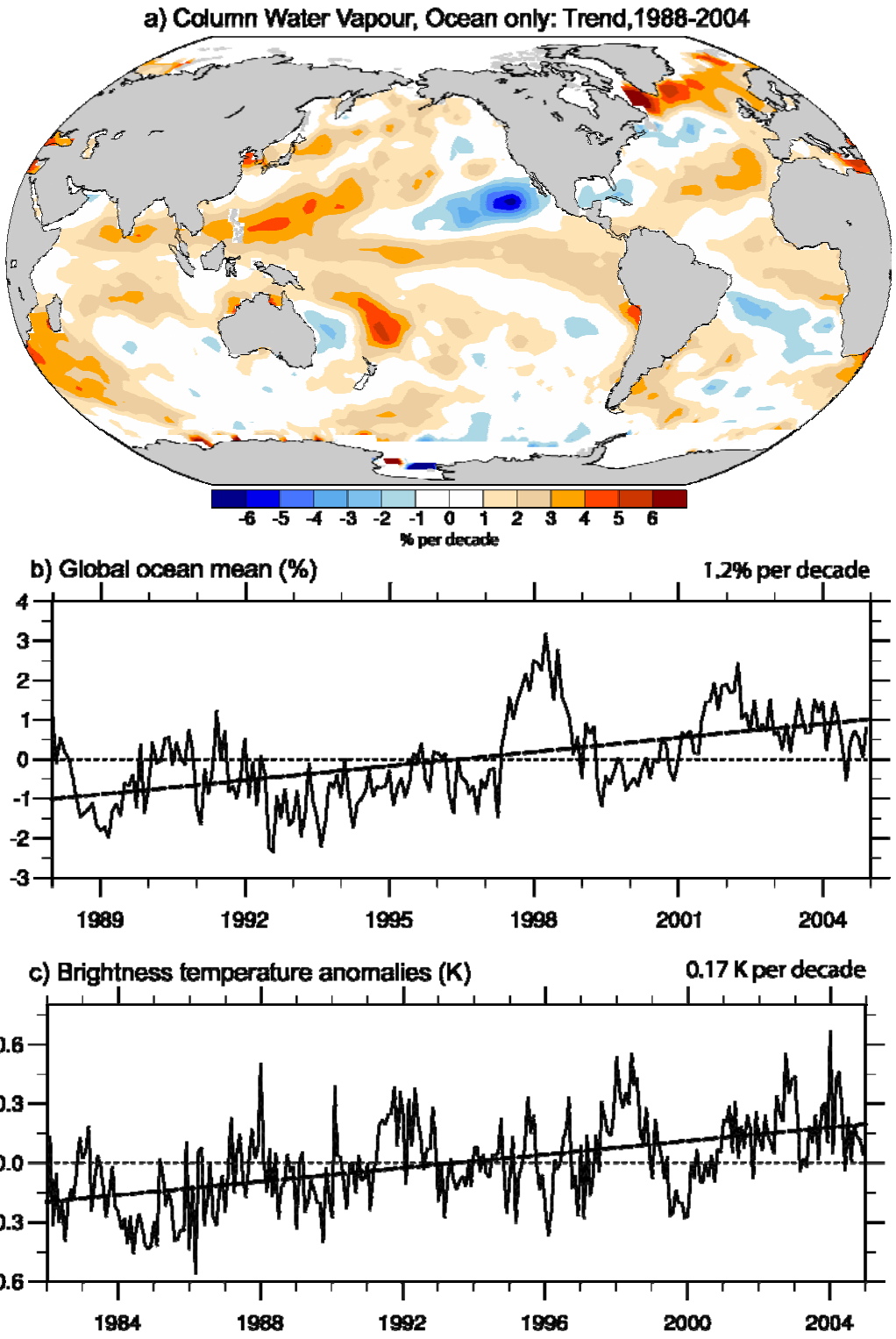

Figure TS-8. Linear trends in precipitable water (total column water vapour) for 1988 to 2004 in % per decade (top panel) and the monthly time series of anomalies over the global ocean plus linear trend (middle panel). The global mean (80°N to 80°S) radiative signature of upper tropospheric moistening is given by monthly time series of combinations of satellite brightness temperature anomalies (°C). The linear trend of the key brightness temperature in °C/decade is also indicated (bottom panel). {see Figure 3.20, Section 3.4, Figure 3.21}

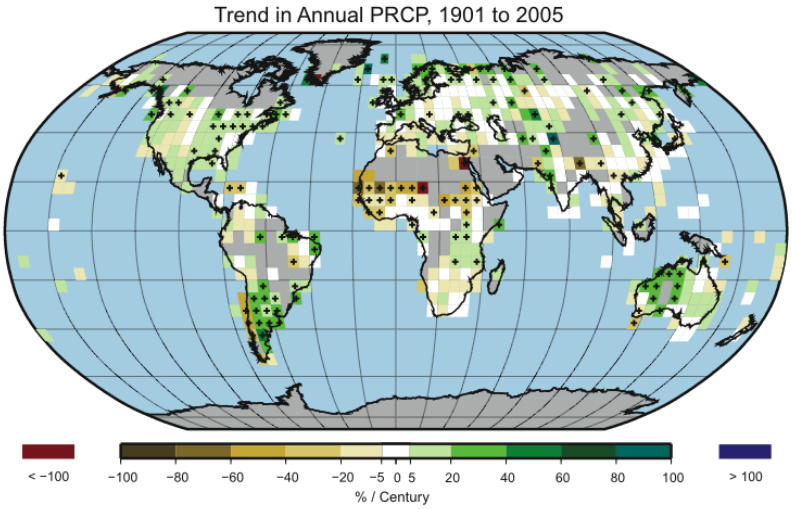

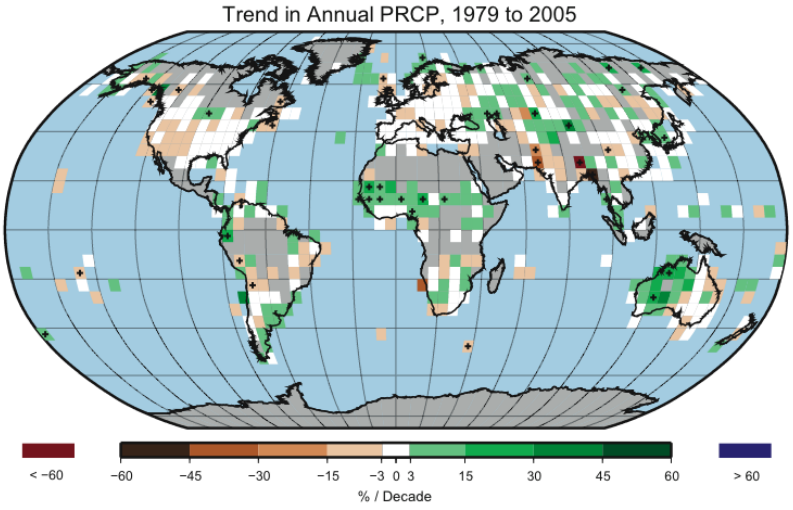

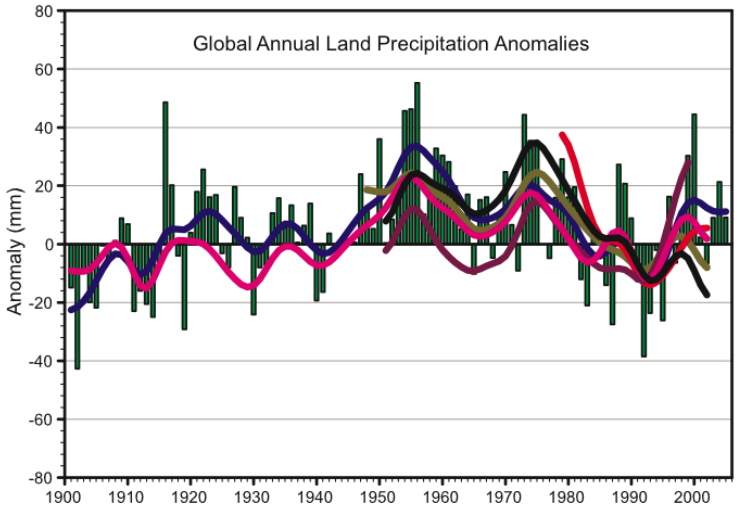

Figure TS-9. *Top and Middle:* Distribution of linear trends of annual land precipitation amounts for 1901–2005 (top) and 1979–2005 (middle). Areas in grey have insufficient data to produce reliable trends. The units are % per century and % per decade as indicated, the percentage being based on the 1961–1990 period. *Bottom:* Time series of annual global land precipitation anomalies with respect to the 1961–1990 base period for 1900 to 2005. Smoothed values from different studies are also indicated, see Section 3.3.2 for details. **{**Figure 3.12 and 3.13}

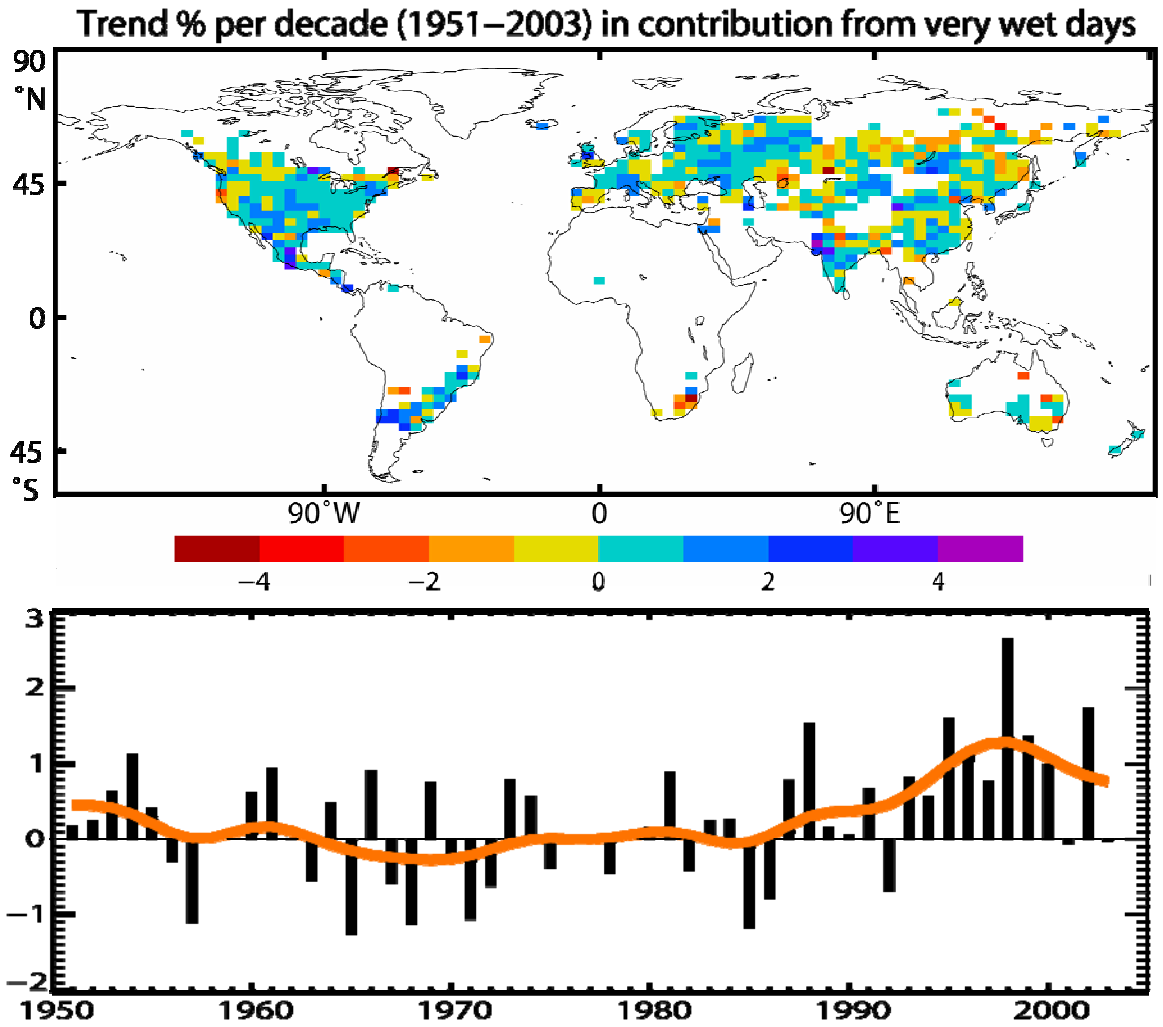

Figure TS-10. *Upper*: Observed trends (%) per decade over 1951–2003 for the contribution to total annual precipitation from very wet days (i.e. corresponding to the 95th percentile and above). White land areas have insufficient data for trend determination. *Lower*: Anomalies of the global (regions of data in top panel) annual time series of very wet days (with respect to 1961–1990) defined as the percentage change from the base period average (22.5%). The orange line shows decadal variations. {Figure 3.39}

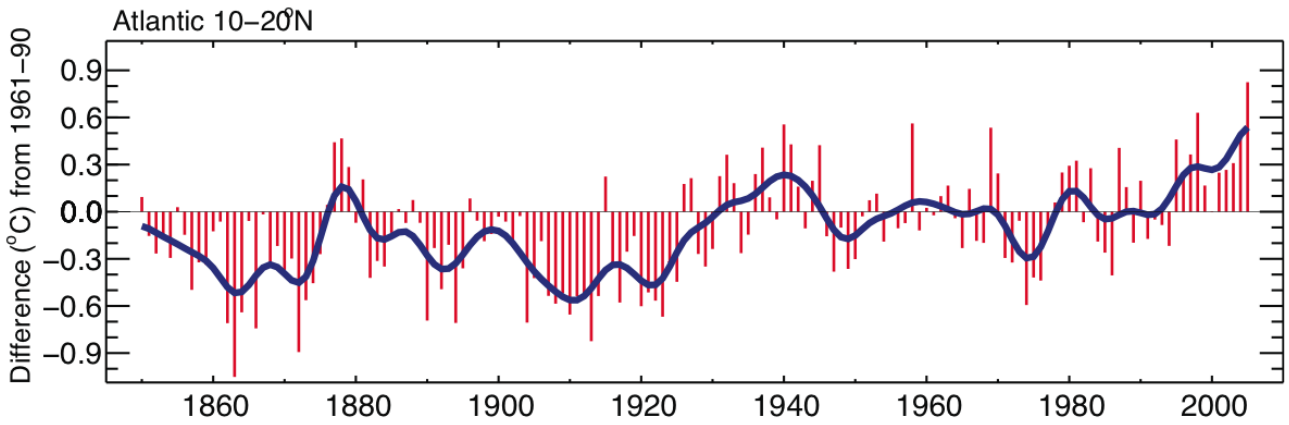

Figure TS-11. Tropical Atlantic (10–20°N) sea surface temperature annual anomalies in the region of Atlantic hurricane formation, relative to 1961–1990 mean (°C). {Figure 3.33}

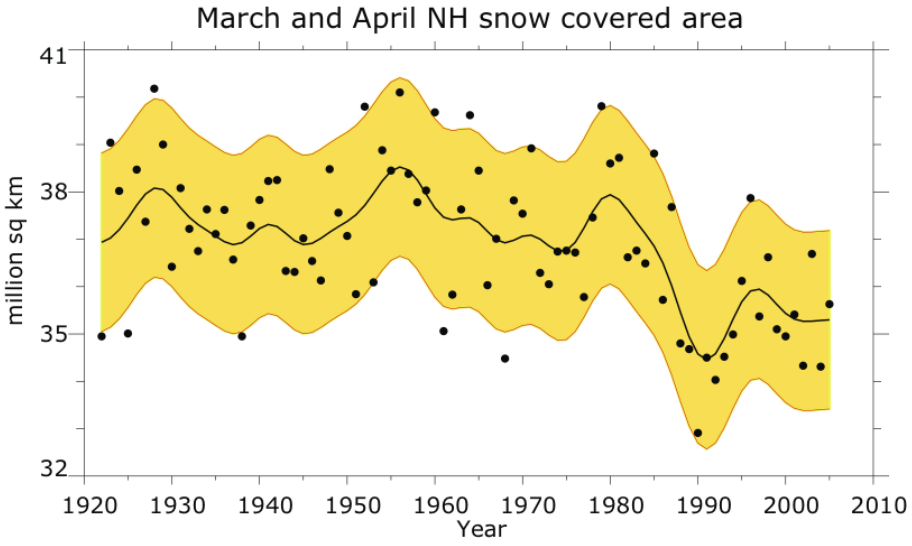

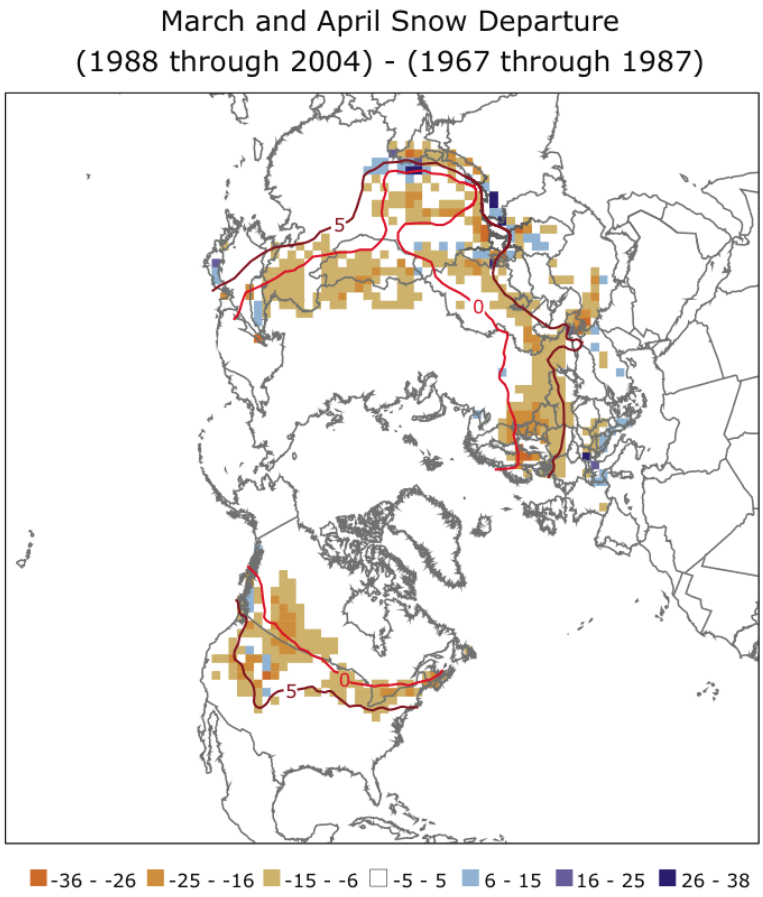

Figure TS-12. *Top*: Northern hemisphere March - April snow cover area from a station-derived snow cover index (prior to 1972) and from satellite data (post 1972). The smooth curve shows decadally averaged values with the 5%–95% data range shown shaded in yellow. *Bottom*: Differences in the distribution of April snow cover between earlier (1967–1987) and later (1988–2004) portions of the satellite era (expressed in percent coverage). Tan colours show areas where snow cover has declined. Most decline occurred between the 0°C and 5°C isotherms shown in red (for April averaged over 1967–2004) owing to strong temperature feedback. {Figures 4.2, 4.3}

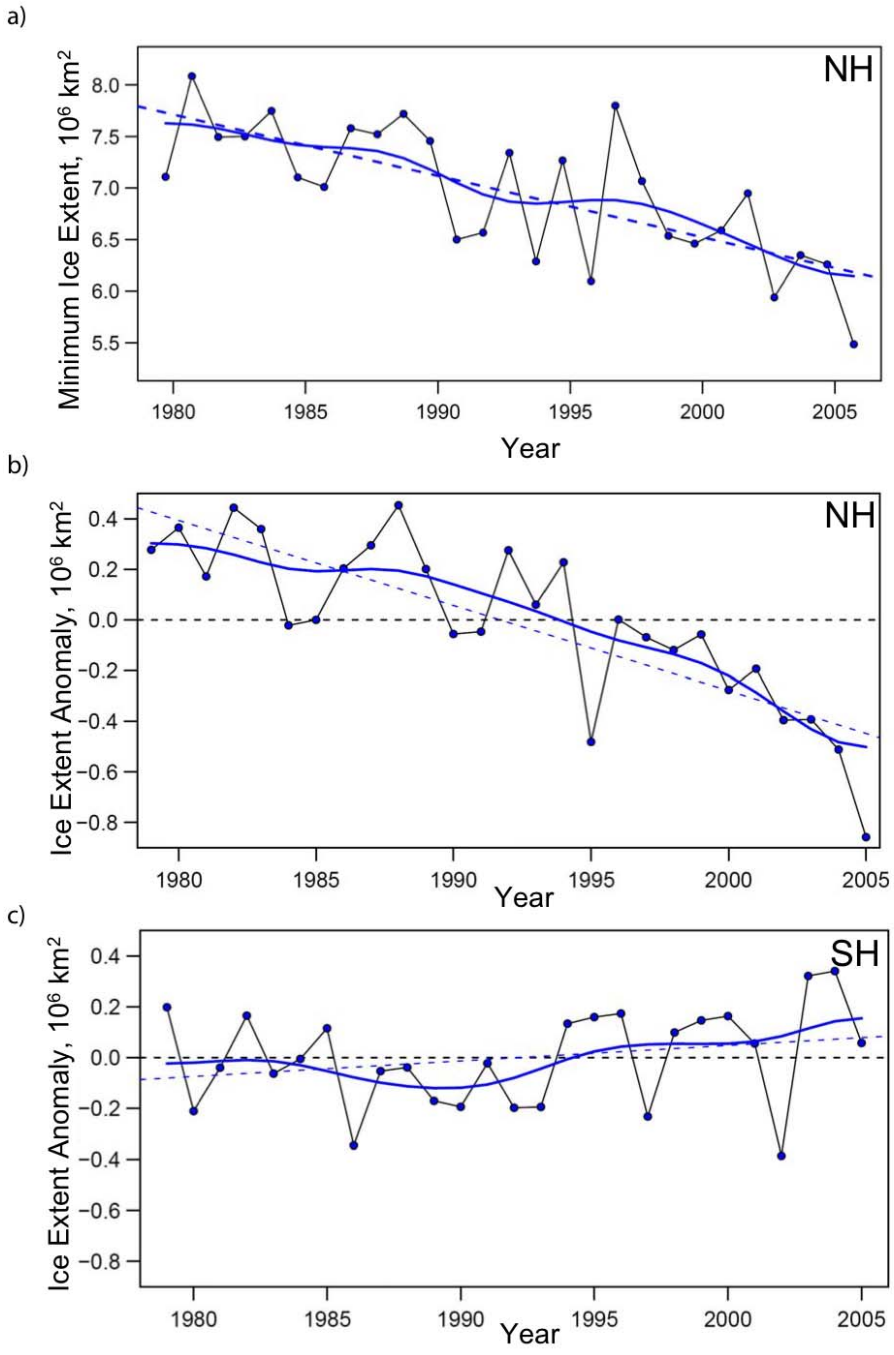

Figure TS-13. (a) Arctic minimum sea ice extent (1979–2005); (b) Arctic sea ice extent anomalies (1979–2005); (c) Antarctic sea ice extent anomalies (1979–2005). Symbols indicate annual values while the curves are the result of a 13-point time filter. The dashed lines indicate the linear trends. (a) Results show a linear trend of –60 ± 24 x 10^3 km^2 year, or approximately –8% per decade. (b) The linear trend is –33 ± 8.8 x 10^3 km^2 yr^{-1} (equivalent to approximately –2.6% per decade) and is significant at the 95% confidence level. (c) Antarctic results show a small positive trend of 5.6 ± 11 x 10^3 km^2 $year^{-1}$ which is not statistically significant. {Figures 4.8 and 4.9}

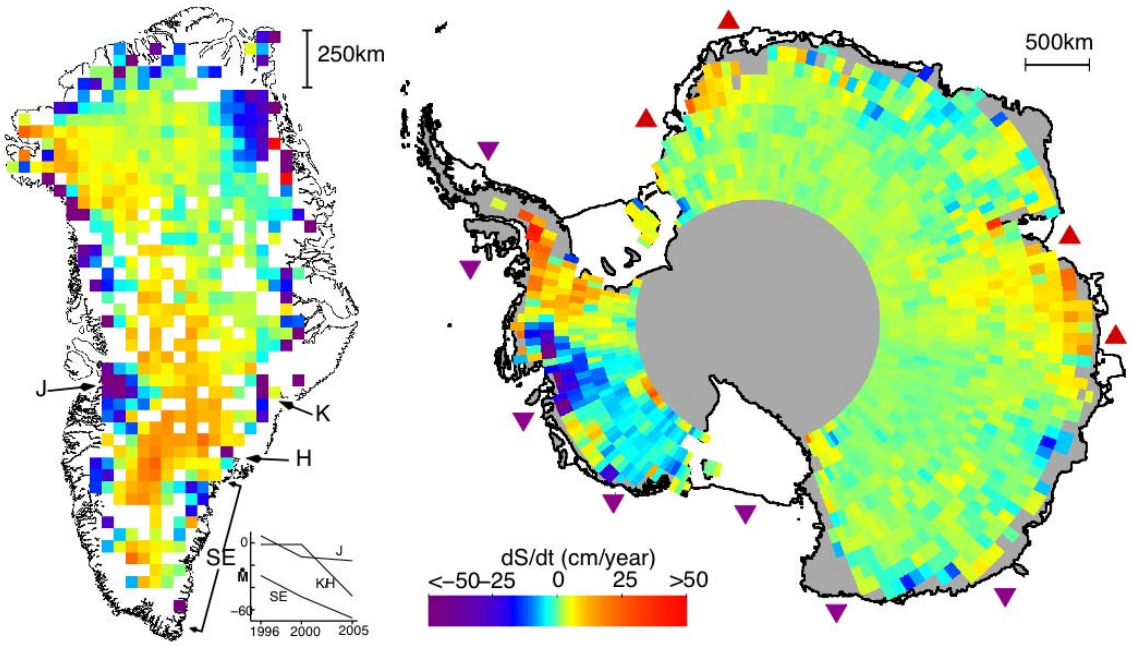

Figure TS-14. Rates of observed recent (1989–2005; 1992–2005) surface-elevation change for Greenland (left) and Antarctica (right), respectively. Red indicates a rising surface and blue a falling surface, which typically indicate increase or loss in ice mass at a site, although changes over time in bedrock elevation and in near-surface density can be important. For Greenland, the rapidly thinning outlet glaciers Jakobshavn (J), Kangerdlugssuaq (K), Helheim (H), and areas along the southeast coast (SE) are shown, together with their estimated mass balance versus time (with K and H combined, in Gt yr^{-1}, with negative values indicating loss of mass from the ice sheet to the ocean. For Antarctica, ice shelves estimated to be thickening or thinning by more than 30 cm yr^{-1} are shown by point-down purple triangles (thinning) and point-up red triangles (thickening) plotted just seaward of the relevant ice shelves. {Figures 4.17 and 4.19}

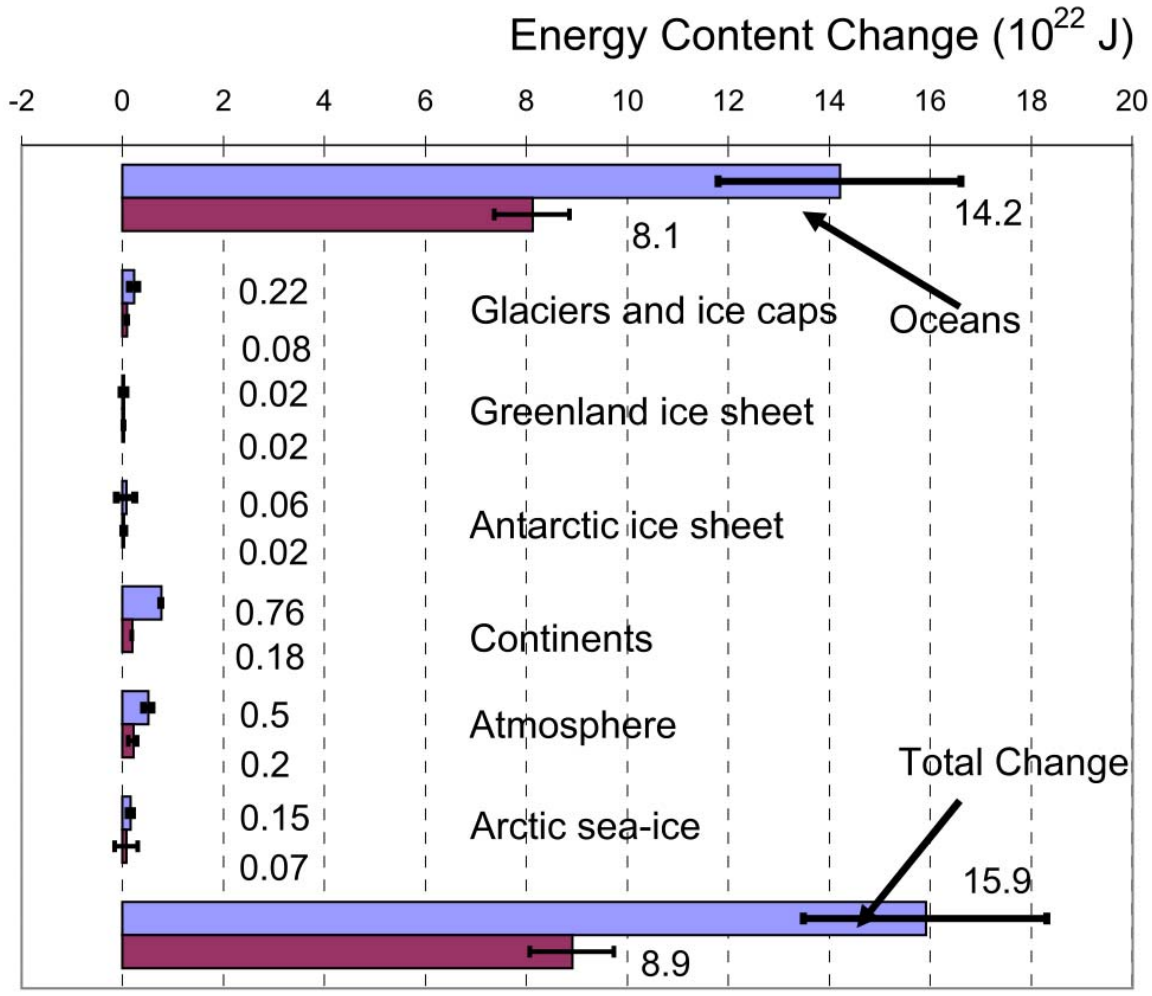

Figure TS-15. Energy content changes in different components of the Earth System for two periods (1961–2003) and (1993–2003). Blue bars are for 1961–2003; burgundy bars are for 1993–2003. Positive energy content change means an increase in stored energy (i.e. heat content in oceans, latent heat from reduced ice or sea-ice volumes, heat content in the continents excluding latent heat from permafrost changes, and latent, sensible heat, potential and kinetic energy for the atmosphere). All error estimates are 90% confidence intervals. No estimate of confidence is available for the continental heat gain. Some of the results have been scaled from published results for the two respective periods. **{**Figure 5.4}

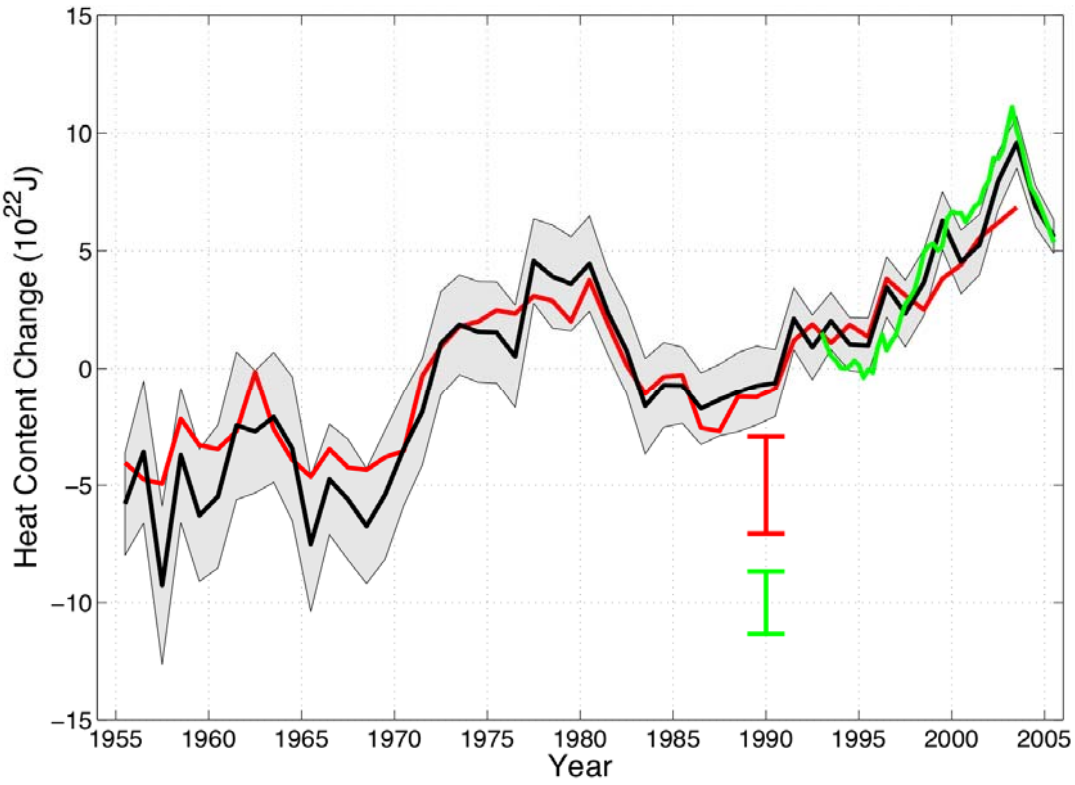

Figure TS-16. Time series of global ocean heat content (10^{22} J) for the 0–700 m layer. The three coloured lines are independent analyses of the oceanographic data. The black and red curves denote the deviation from their 1961–1990 average and the shorter green curve the deviation from the average of the black curve for the period 1993–2003. The 90% uncertainty range for the black curve is indicated by the grey shading and for the other two curves by the error bars {Figure 5.1}.

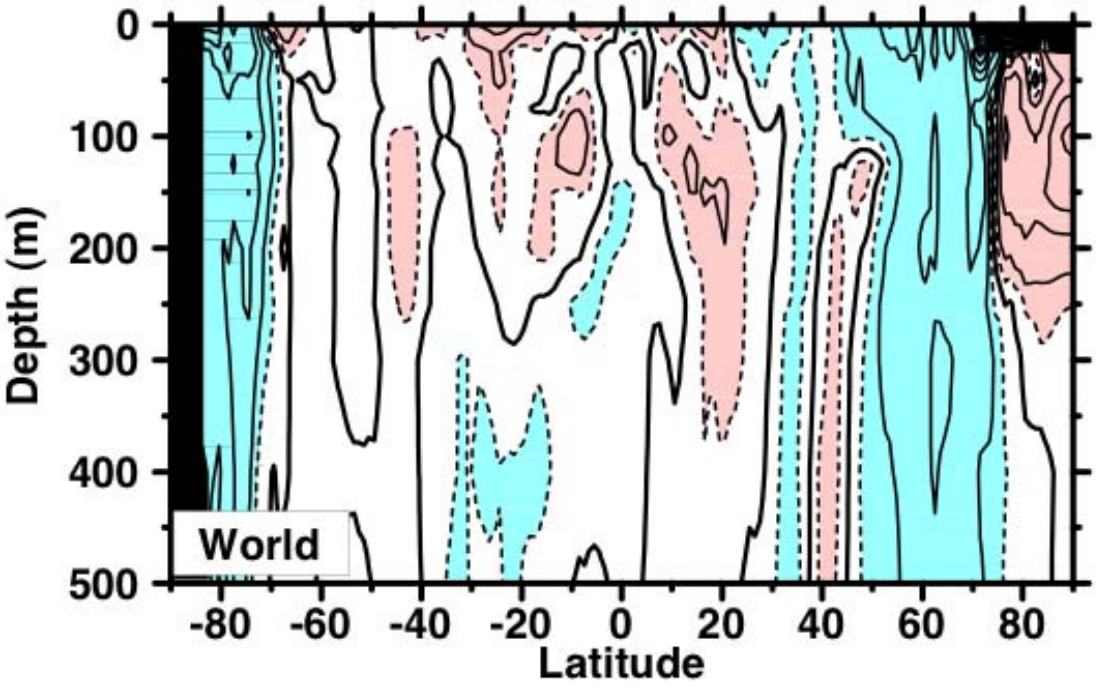

Figure TS-17. Linear trends (1955–1998) of zonally averaged salinity (Practical Salinity Scale) for the World Ocean. Contour interval is 0.01 per decade and dashed contours are ±0.005 per decade. Dark, solid line is the zero contour. Red shading indicates values equal or greater than 0.005 per decade and blue shading indicates values equal or less than –0.005 per decade. {Figure 5.5}

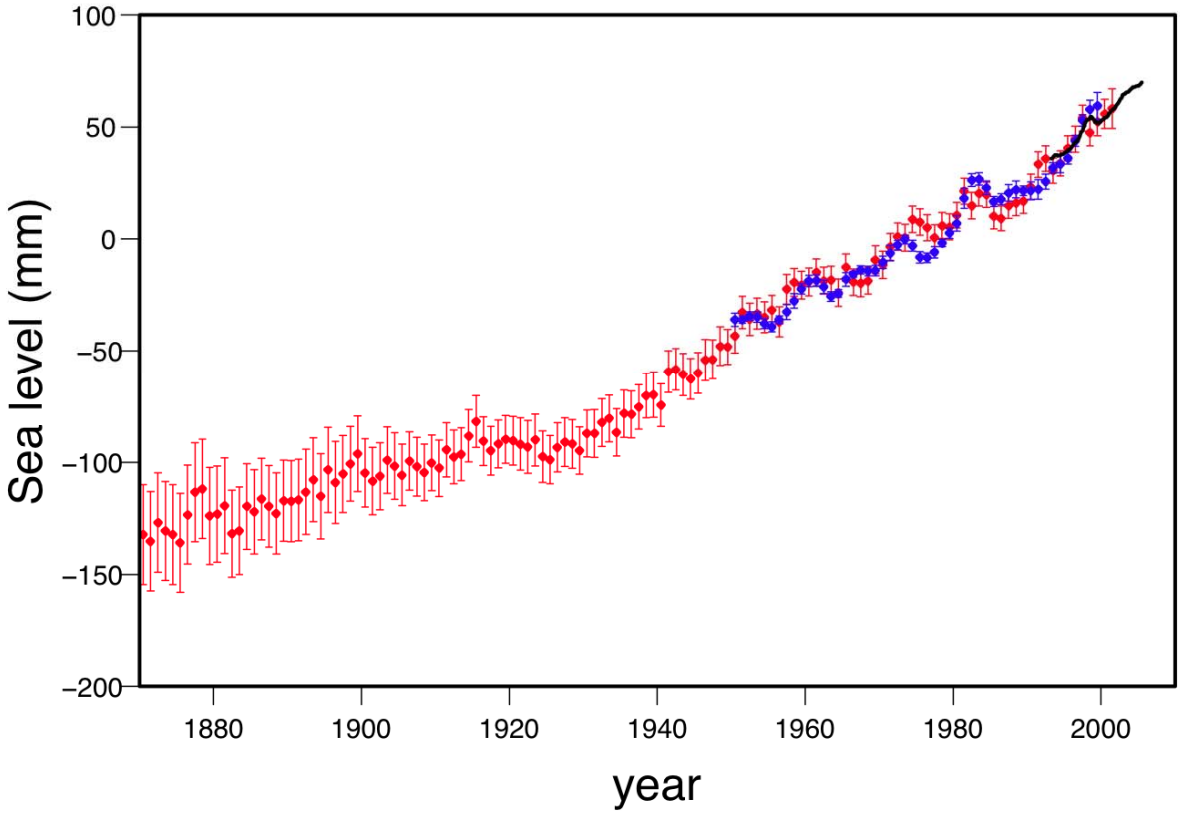

Figure TS-18. Annual averages of the global mean sea level based on reconstructed sea level fields since 1870 (red), tide gauge measurements since 1950 (blue), and satellite altimetry since 1992 (black). Units are in mm relative to the average for 1961–1990. Error bars are 90% confidence intervals. {Figure 5.13}

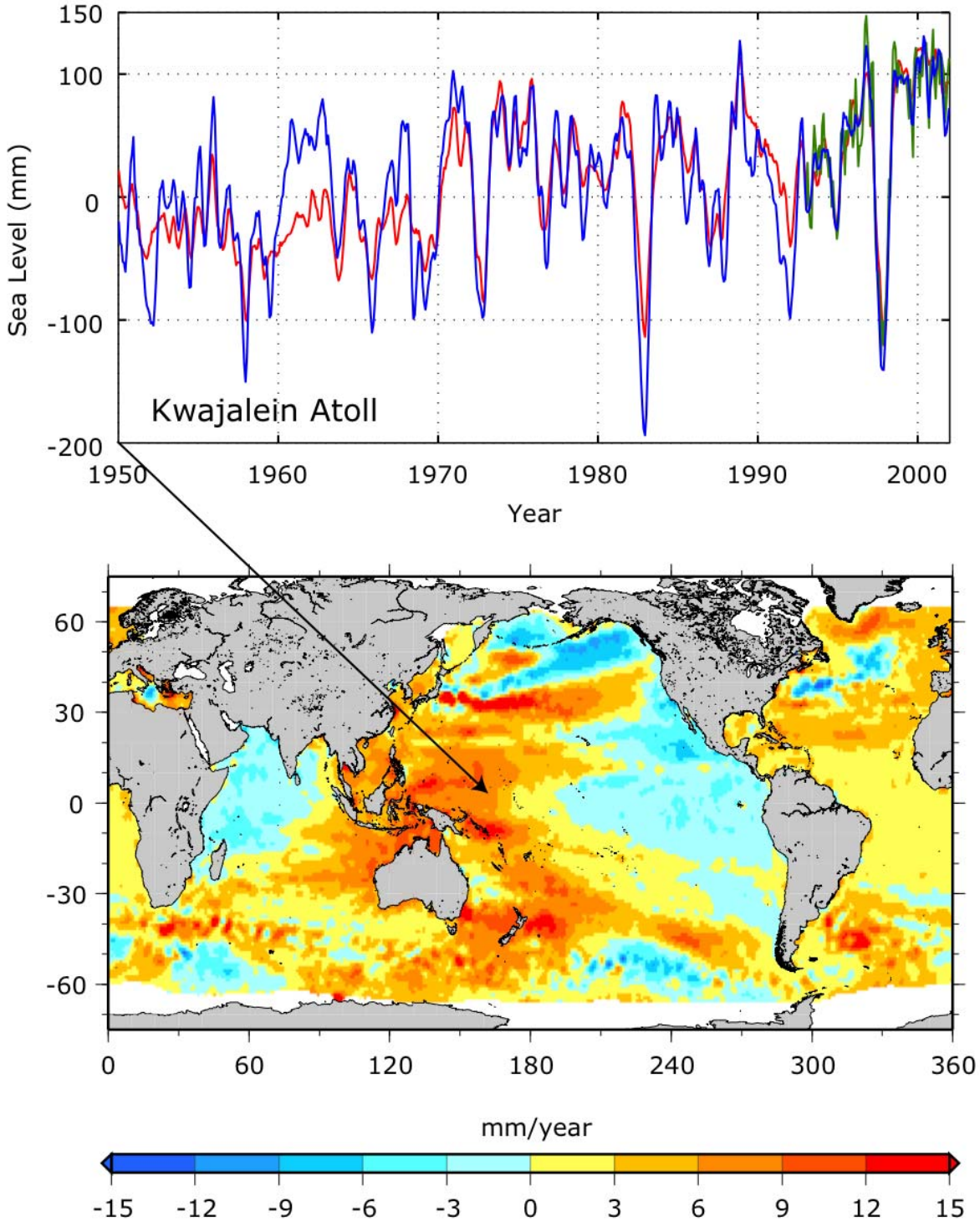

Figure TS-19. *Top*: Monthly mean sea level curve for 1950–2000 at Kwajalein (8°44'N, 167°44'E). The observed sea level (from tide gauge measurements) is in blue, the reconstructed sea level in red, and the satellite altimetry record in green. Annual and semi-annual signals are removed from each time series and the tide gauge data has been smoothed. {Figure 5.18} *Bottom*: Geographic distribution of short term linear trends in mean sea level for 1993–2003 based on TOPEX/Poseidon satellite altimetry. Units are in mm yr^{-1}. {Figure 5.15}

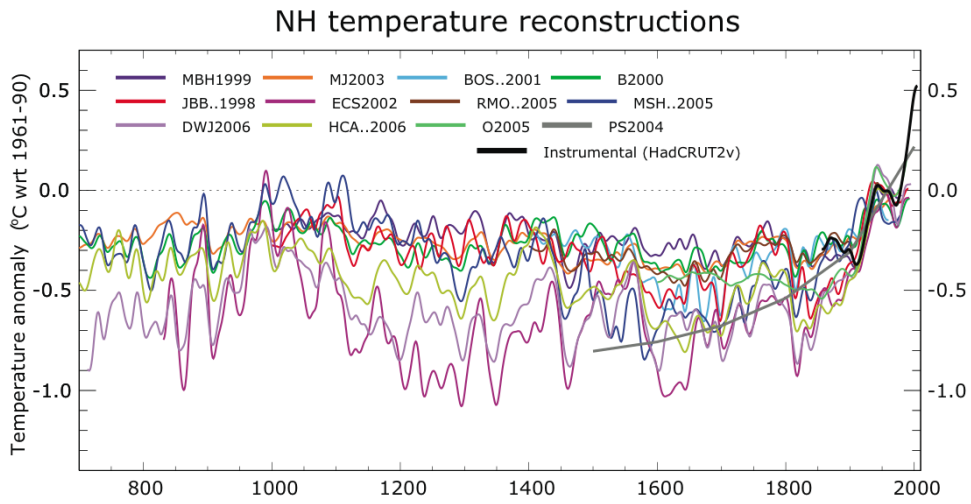

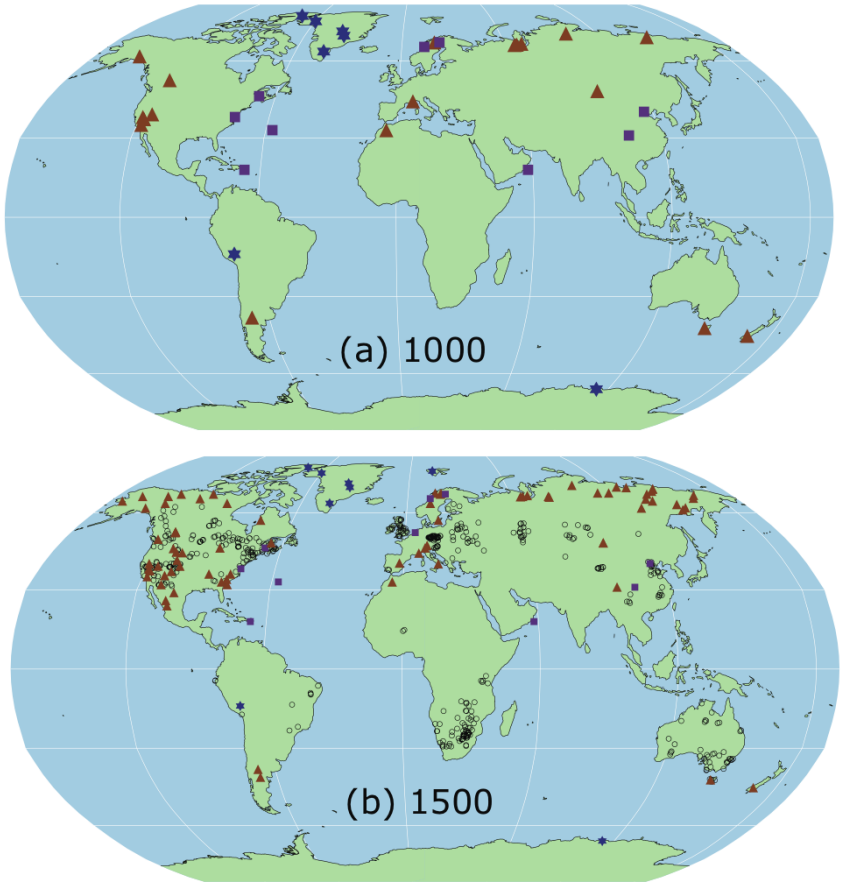

Figure TS-20. *Top*: Records of Northern Hemisphere (NH) temperature variation during the last 1300 years showing twelve reconstructions using multiple climate proxy records shown in colour and instrumental records shown in black. *Middle and Bottom*: Locations of temperature-sensitive proxy records with data back to 1000 AD and 1500 AD (tree-rings: brown triangles; boreholes: black circles; ice-core/ice-boreholes: blue stars; other records including low-resolution records: purple squares). Data sources are given in Table 6.1, Figure 6.10 and are discussed in Chapter 6. {Figures 6.10 and 6.11}

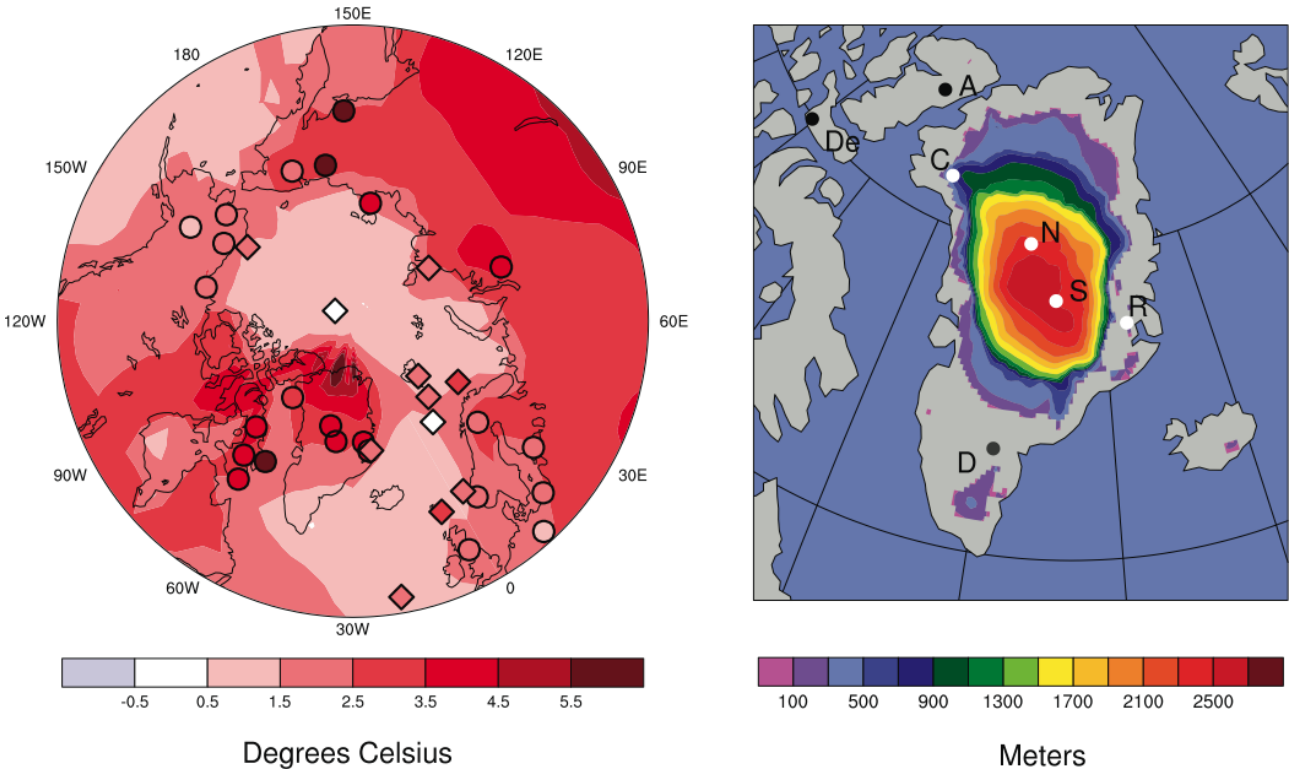

Figure TS-21. Summer surface air temperature change relative to the present over the Arctic as well as annual ice thickness and extent for Greenland and western Arctic glaciers for the Last Interglacial, approximately 125 kyr ago, from a multi-model and a multi-proxy synthesis. *Left:* The summer warming simulated by the NCAR CCSM and ECHO-G model is contoured and is overlain by proxy estimates of maximum summer warming from terrestrial (circles) and marine (diamonds) sites. *Right:* Extents and thicknesses of the Greenland ice sheet and western Canadian and Iceland glaciers are shown at their minimum extent for the Last Interglacial as a multi-model average from three ice models. Ice core observations indicate LIG ice (white dots) at Renland (R), NGRIP (N), Summit (S, GRIP and GISP2), and possibly Camp Century (C), but no LIG ice (black dots) at Dye-3 (D), Devon (De), and Agassiz (A). {Figure 6.6}

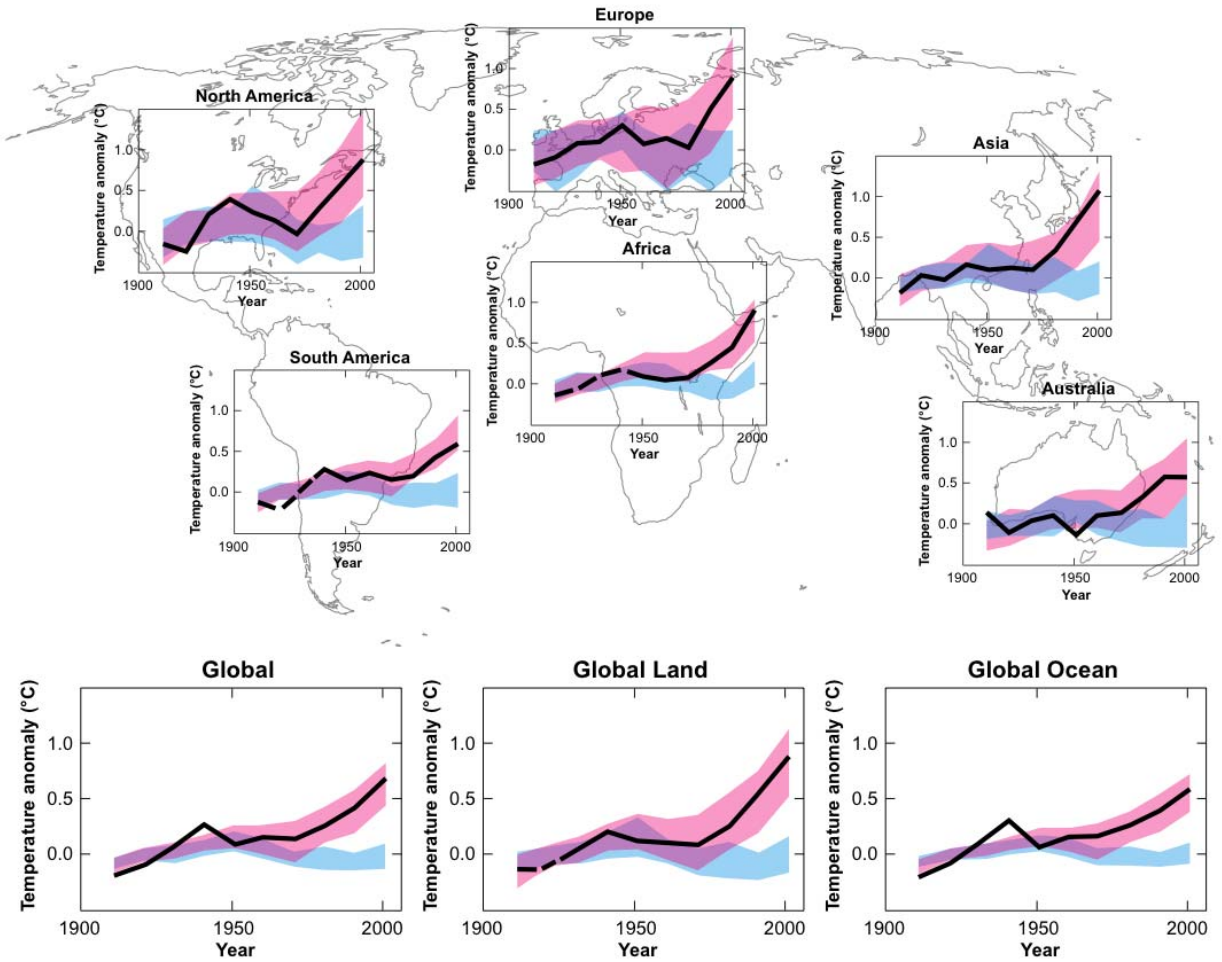

Figure TS-22. Continental, global, global land, and global ocean decadal mean temperature anomalies relative to the period 1901–1950. The black lines show observed temperature anomalies. Dashed black lines indicate decades and continental regions for which the available spatial coverage is less than 50% of the total area. The red bands represent approximately the middle 90% for simulations of 20th century climate with prescribed anthropogenic and natural forcings. The blue bands similarly represent the rage of simulations with prescribed natural forcings only. The model data were masked with the pattern of observed missing data and were subsequently processed identically to the observations. Data sources and models used are described in Section 9.4, FAQ 9.2, Table 8.1 and supplementary information for Chapter 9. {FAQ 9.2, Figure 1}

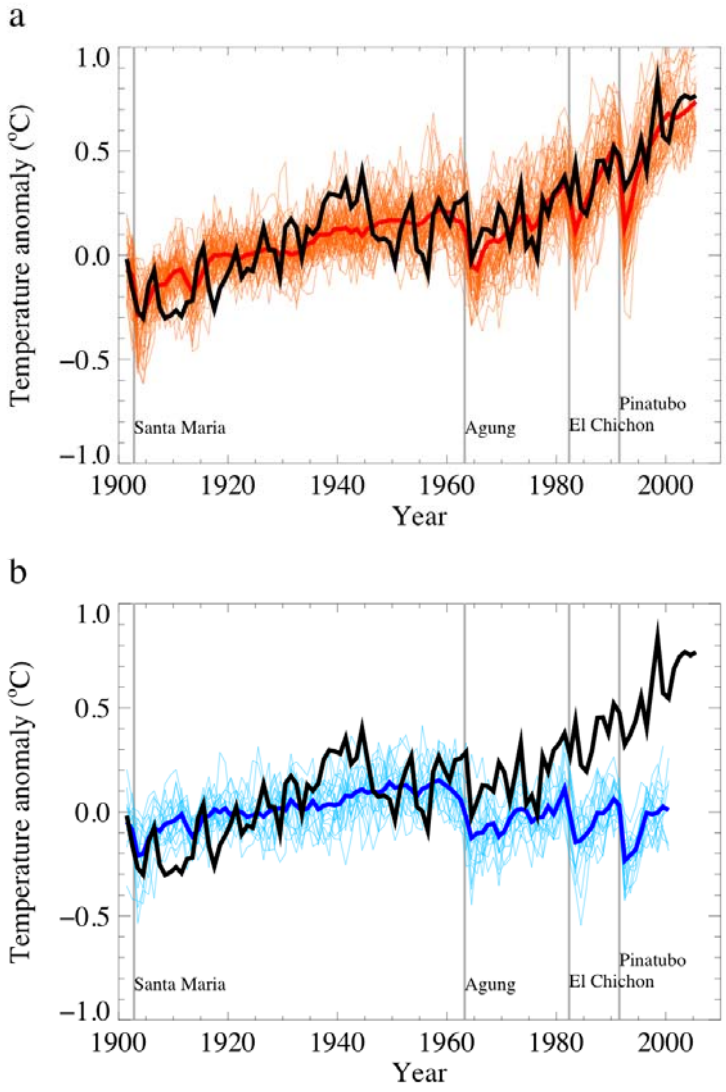

Figure TS-23. (a) Global mean surface temperature anomalies relative to the period 1901–1950, as observed (black line) and as obtained from simulations with both anthropogenic and natural forcings. The multimodel ensemble mean is shown as a thick red curve and individual simulations are shown as thin red curves. Vertical grey lines indicate the timing of major volcanic events. (b) As (a), except that the simulated global mean temperature anomalies are for natural forcings only. The multimodel ensemble mean is shown as a thick blue curve and individual simulations are shown as thin blue curves. The simulations are selected as for Figure TS-22. Each simulation was sampled so that coverage corresponds to that of the observations. Further details of the methodology for producing this figure are given in the supplementary information for Chapter 9. {Figure 9.5}

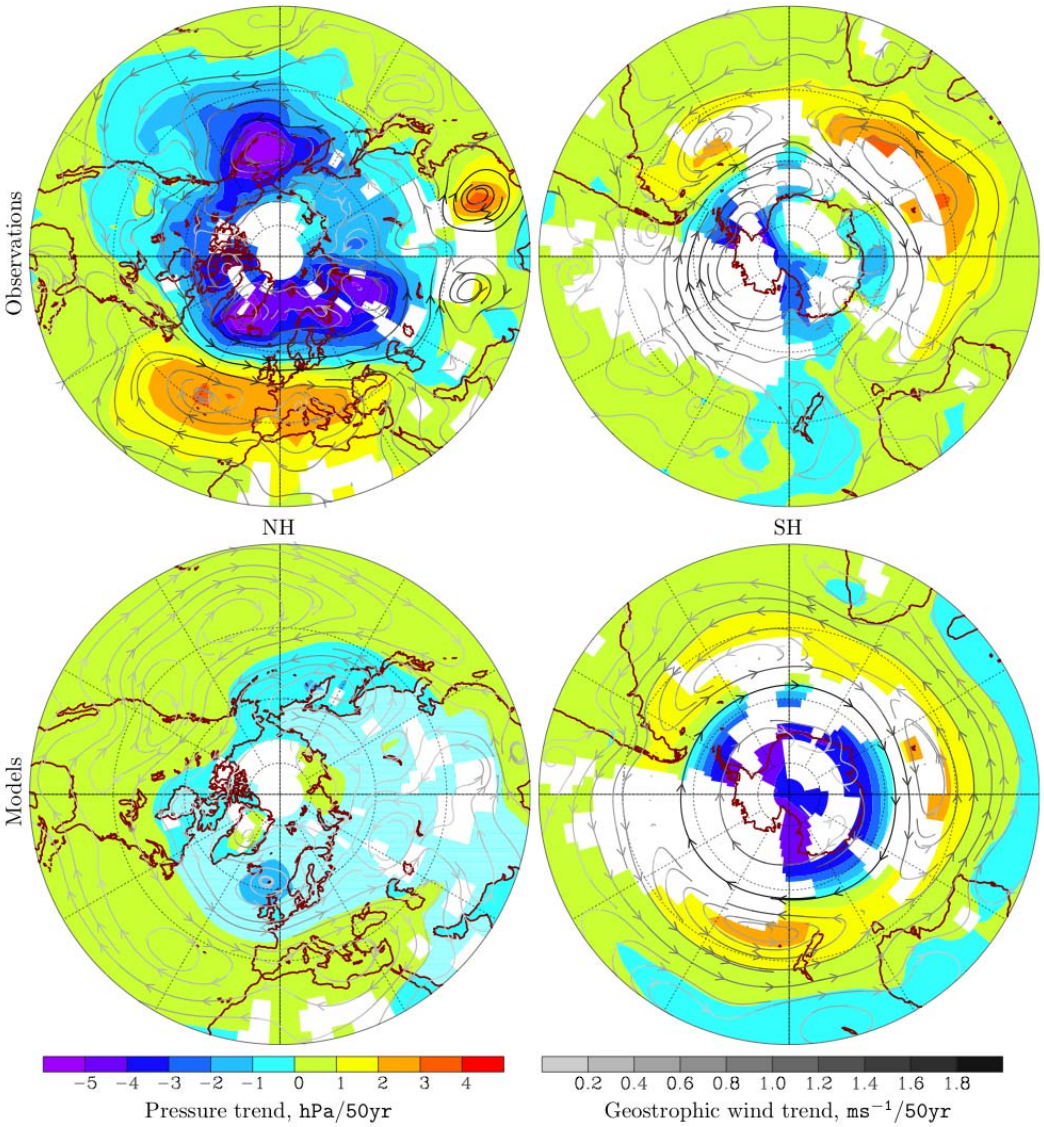

Figure TS-24. December-February sea-level pressure trends based on decadal means for the period 1955–2005. Top panels: Observed trends estimated from an observational dataset and displayed in regions where there is observational coverage. Bottom panels: Mean trends simulated in response to natural and anthropogenic forcing changes in eight coupled models. The model simulated trends are displayed only where observationally based trends are displayed. Streamlines, which are not masked, indicate the direction of the trends in the geostrophic wind derived from the trends in sea-level pressure, and the shading of the streamlines indicates the magnitude of the change, with darker streamlines corresponding to larger changes in geostrophic wind. Data sources and models are described in Chapter 9 and its supplementary material. Model details are provided in Table 8.1. {Figure 9.16}

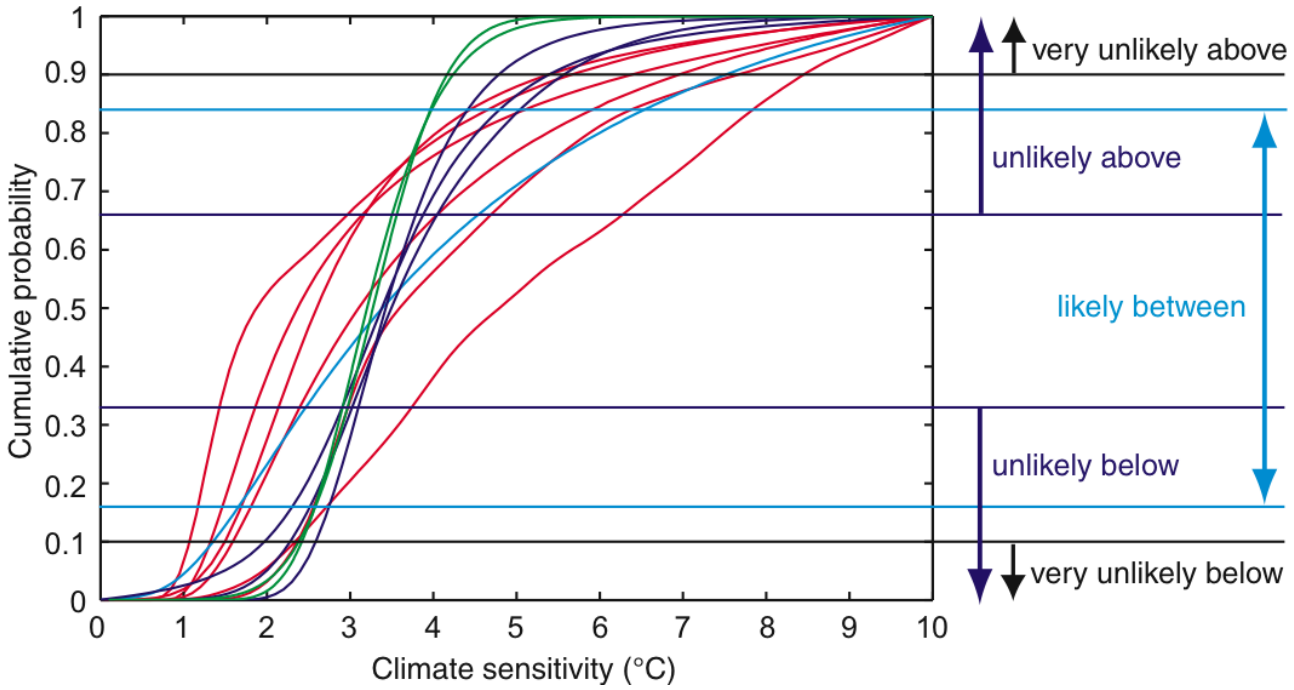

Figure TS-25. Cumulative distributions of climate sensitivity derived from: observed 20th century warming (red), model climatology (blue), proxy evidence (cyan) and from climate sensitivities of AOGCMs (green). Horizontal lines and arrows mark the boundaries of the likelihood estimates defined in the IPCC AR4 Uncertainty Guidance Note. {Box 10.2, Figures 1 and 2}

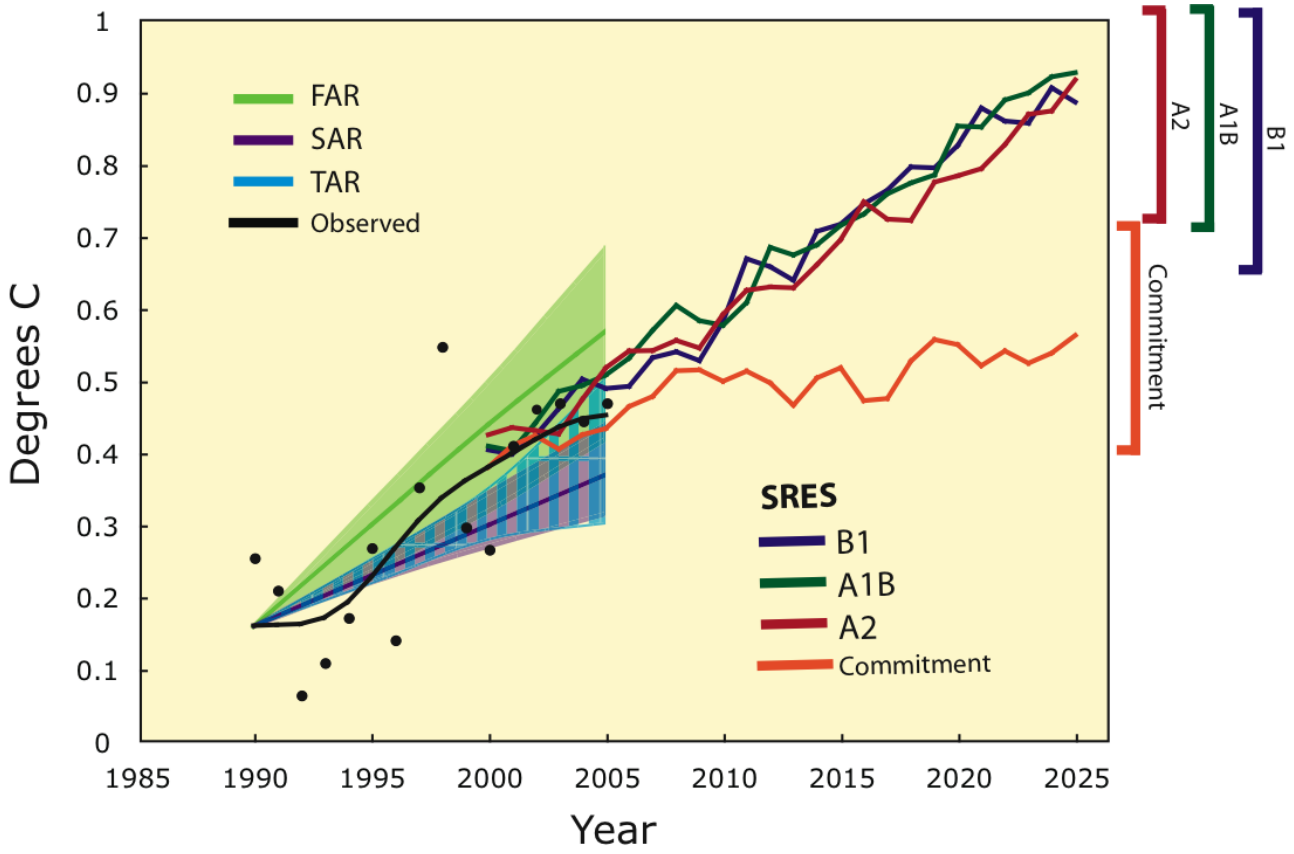

Figure TS-26. Model projections of global mean warming compared to observed warming. Observed temperature anomalies, as in Figure TS-6, are shown as annual (black dots) and decadal average values (black line). Projected trends and their ranges from the IPCC First (FAR) and Second (SAR) Assessment Reports are shown as green and magenta solid lines and shaded areas, and the projected range from the TAR is shown by vertical blue bars. These projections are adjusted to start at the observed decadal average value in 1990. Multi-model mean projections from this report for the SRES B1, A1B and A2 scenarios, as in Figure TS-32, are shown for the period 2000 – 2025 as blue, green and red curves with uncertainty ranges indicated against the right hand axis. The orange curve shows model projections of warming if greenhouse gas and aerosol concentrations were held constant from year 2000 – i.e., the constant forcing commitment. {Figures 1.1 and 10.4}

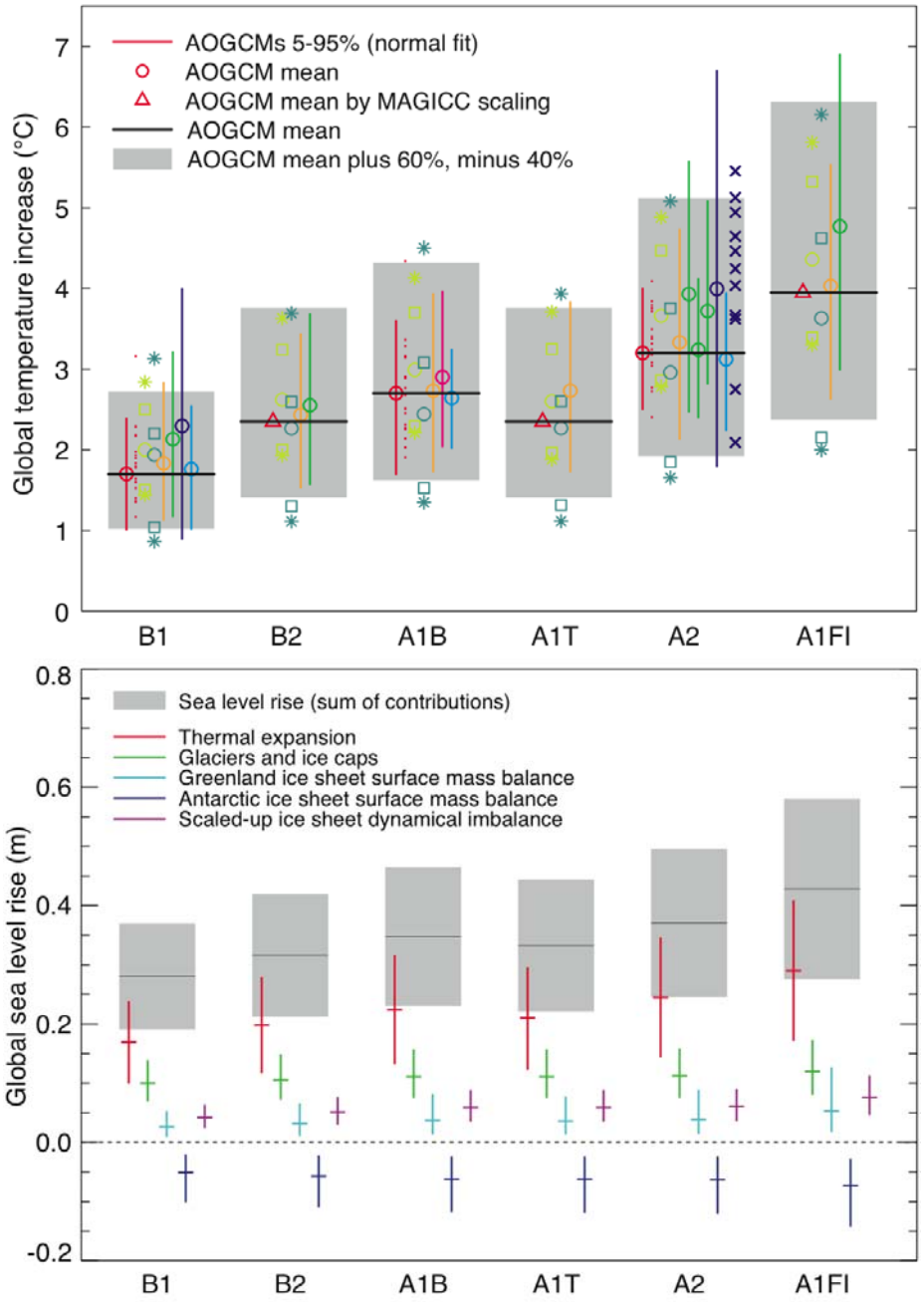

Figure TS-27. *Top:* Projected global mean temperature change in 2090–2099 relative to 1980–1999. for the six SRES marker scenarios based on results from different and independent models. The multi-model AOGCM mean, and the range of the mean minus 40% to plus 60% are shown as black horizontal solid lines and grey bars, respectively. Carbon cycle uncertainties are estimated for scenario A2 based on C4MIP models (dark blue crosses), and for all marker scenarios using the Bern2.5CC EMIC (pale blue symbols). Other symbols represent individual studies, see Figure 10.29 for details. *Bottom:* Projected global average sea level rise and its components in 2090–2099 (relative to 1980–1999) for the six SRES marker scenarios. The uncertainties denote 5–95% ranges, based on the spread of model results, and not including carbon-cycle uncertainties. The contributions are derived by scaling AOGCM results and estimating land ice changes from temperature changes (see Appendix 10.A for details). Individual contributions are added to give the total sea level rise, which does not include the contribution shown for ice sheet dynamical imbalance, for which the current level of understanding prevents a best estimate from being given. {Figures 10.29 and 10.33}

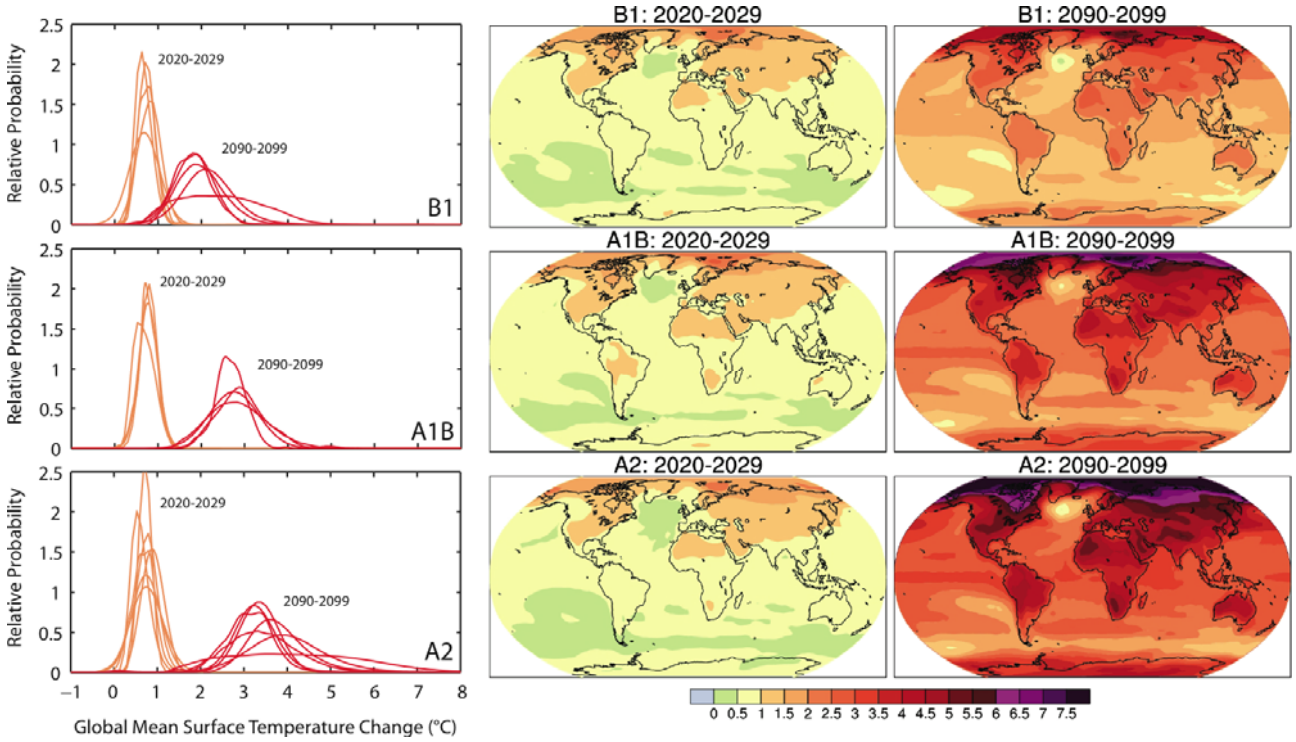

Figure TS-28. Projected global average temperature changes for the early and late 21st century relative to the period 1980–1999. The central and right panels show the multi-model average projections for the B1 (top), A1B (middle) and A2 (bottom) SRES scenarios averaged over decades 2020–2029 (centre) and 2090–2099 (right). The left panel shows corresponding uncertainties as the relative probabilities of estimated global average warming from several different studies for the same periods. {Figures 10.8 and 10.28}

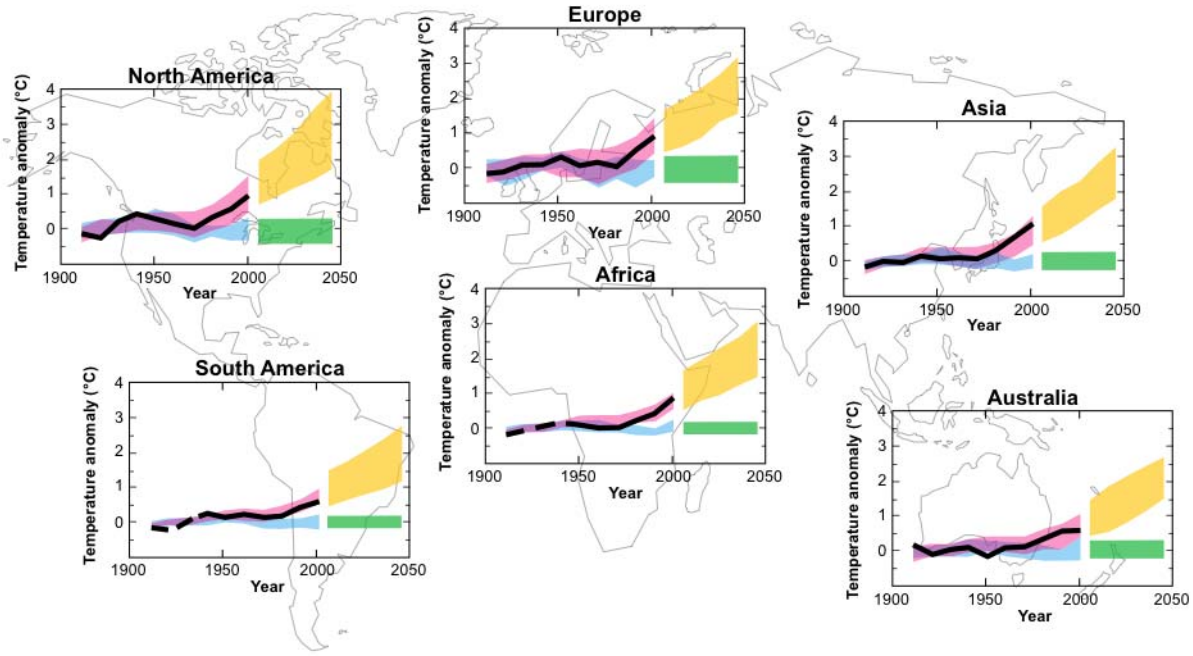

Figure TS-29. Decadal mean continental surface temperature anomalies in observations and simulations for the period 1906 to 2005 and in projections for 2001–2050. Anomalies are calculated from the 1901-1950 average. The black lines represent the observations and the red and blue bands show simulated average temperature anomalies as in Figure TS-25 for the 20th century, i.e. including anthropogenic and natural forcings or only natural forcings respectively. The orange shading represents the 5th-95th percentile range of projected changes according to the IPCC SRES A1B emissions scenario. The green bar denotes the 5th–95th percentile range of decadal mean anomalies from the 20th century simulations with only natural forcings, i.e. a measure of the natural decadal variability. For the observed part of these graphs, the decadal averages are centred on calendar decade boundaries, i.e. the last point is at 2000 for 1996–2005, whereas for the future period they are centred on calendar decade mid-points, i.e. the first point is at 2005 for 2001–2010. To construct the ranges all simulations from the set of models involved were considered independent realisations of the possible evolution of the climate given the forcings applied. This involved 58 simulations from 14 models for the red curve, 19 simulations from 5 models (a subset of the 14) for the blue curve and green bar and 47 simulations from 18 models for the orange curve. {FAQ 9.2.1, Figure 1 and Box 11.1, Figure 1}

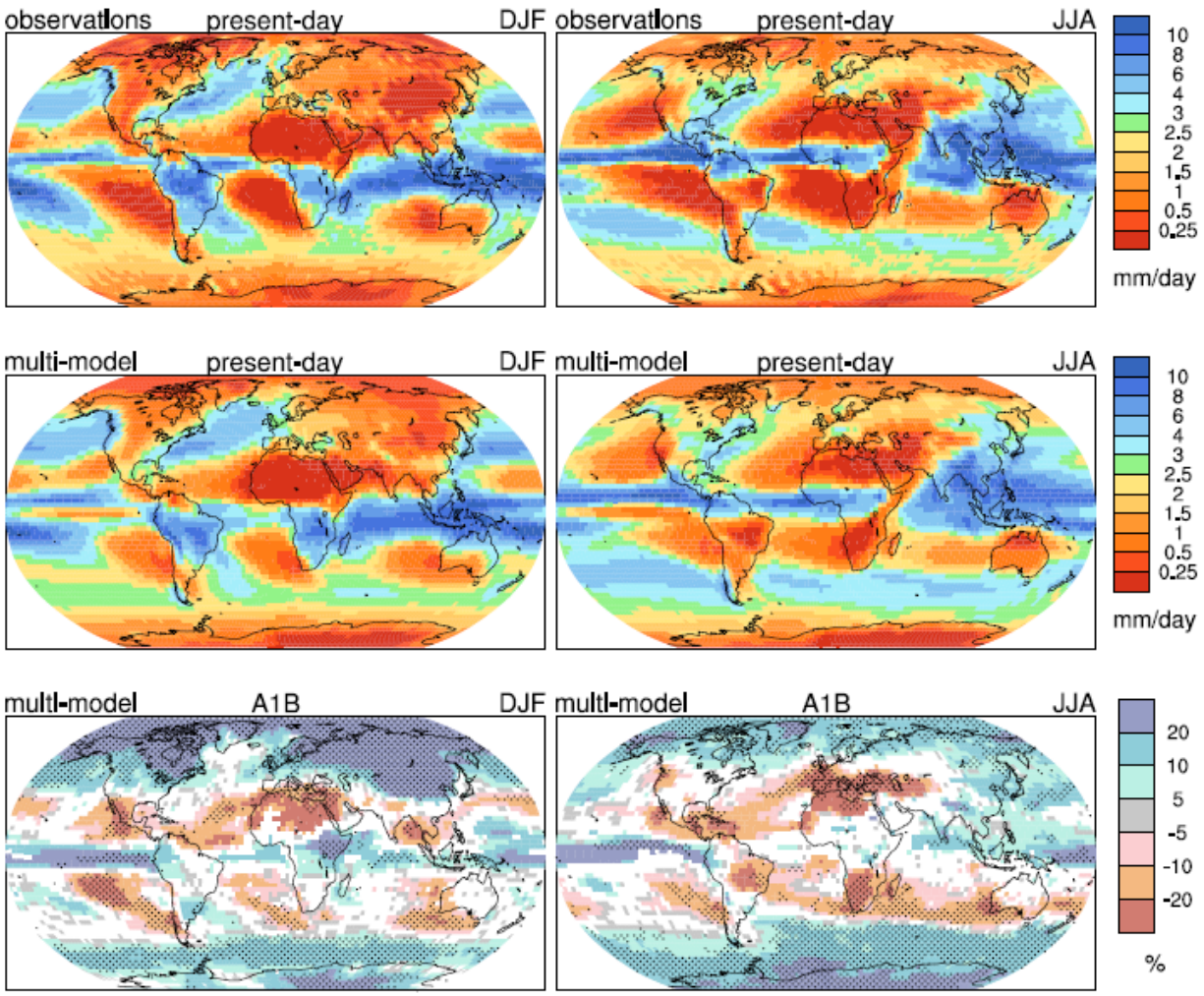

Figure TS-30. Spatial patterns of observed (top row) and multi-model mean (middle row) seasonal mean precipitation rate for the period 1979–1993 and the multi-model mean for changes by the period 2090–2099 relative to 1980–1999 based on the SRES A1B scenario (bottom row). December to February means are in the left column, June to August means in the right column. Units are mm per day (top two rows) or percent change (bottom row). In the bottom panel changes are plotted only where more than 66% of the models agree in the sign of the change. The stippling indicates areas where more than 90% of the models agree in the sign of the change. {Figure 10.9}

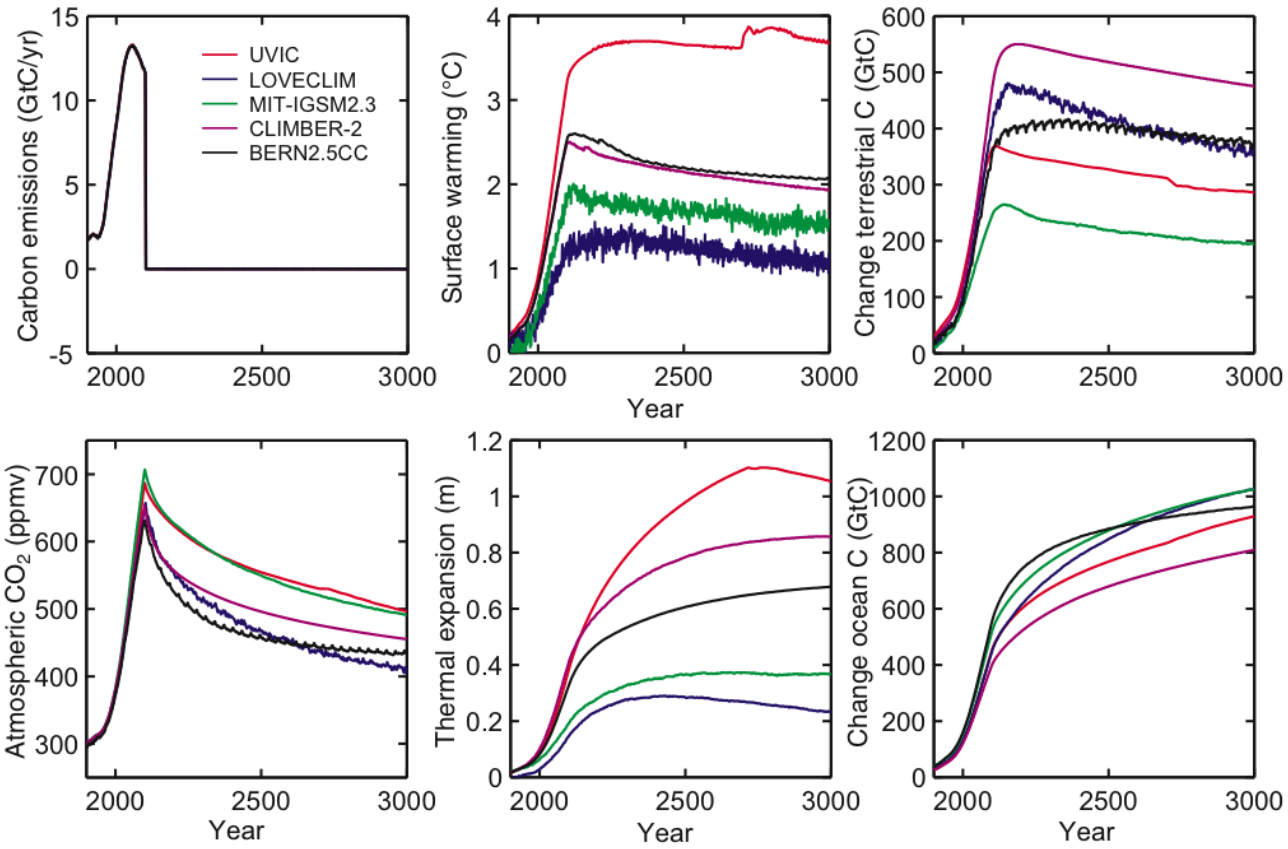

Figure TS-31. Calculation of climate change commitment due to past emissions for five different intermediate complexity models and an idealized scenario where emissions follow a pathway leading to stabilization of atmospheric CO_2 at 750 ppm, but before reaching this target, emissions are reduced to zero instantly at year 2100. *Left column:* CO_2 emissions and atmospheric CO_2 concentrations. *Center column:* surface warming and sea level rise due to thermal expansion; *Right column:* change in total terrestrial and oceanic carbon inventory since preindustrial time. {Figure 10.35}

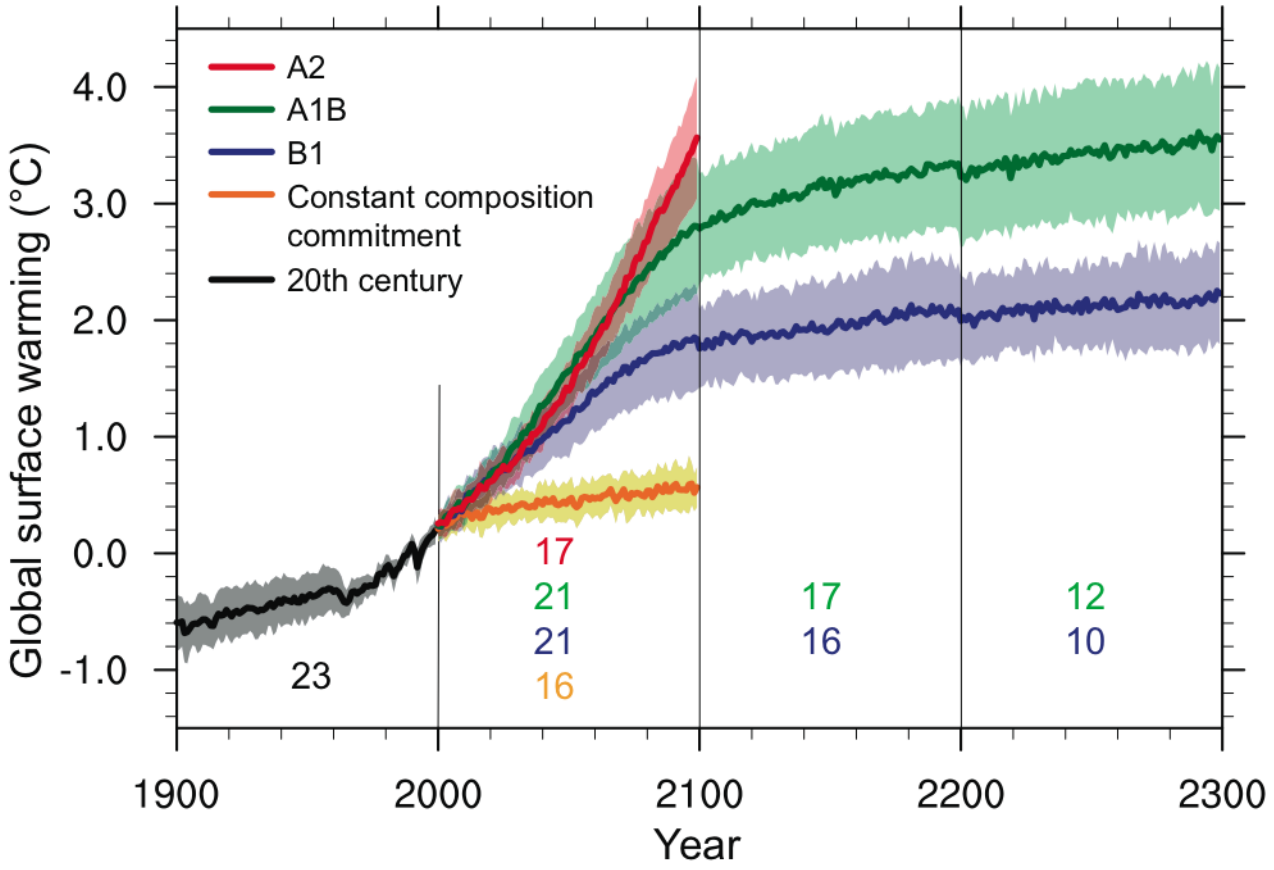

Figure TS-32. Multi-model means of surface warming (compared to the 1980–1999 base period) for the SRES scenarios A2 (red), A1B (green) and B1 (blue), shown as continuations of the 20th century simulation. The latter two scenarios are continued beyond year 2100 with forcing kept constant (climate change commitment, see Box TS.5.2). An additional experiment, in which the forcing is kept at the year 2000 level, illustrates committed warming. Linear trends from the corresponding control runs have been removed from these time series. Lines show the multi model means, shading denotes the plus/ minus one standard deviation range. Discontinuities between different periods have no physical meaning and are caused by the fact that the number of models that have run a given scenario is different for each period and scenario (numbers indicated in figure). For the same reason, uncertainty across scenarios should not be interpreted from this figure (see Section 10.5 for uncertainty estimates). {Figure 10.4}

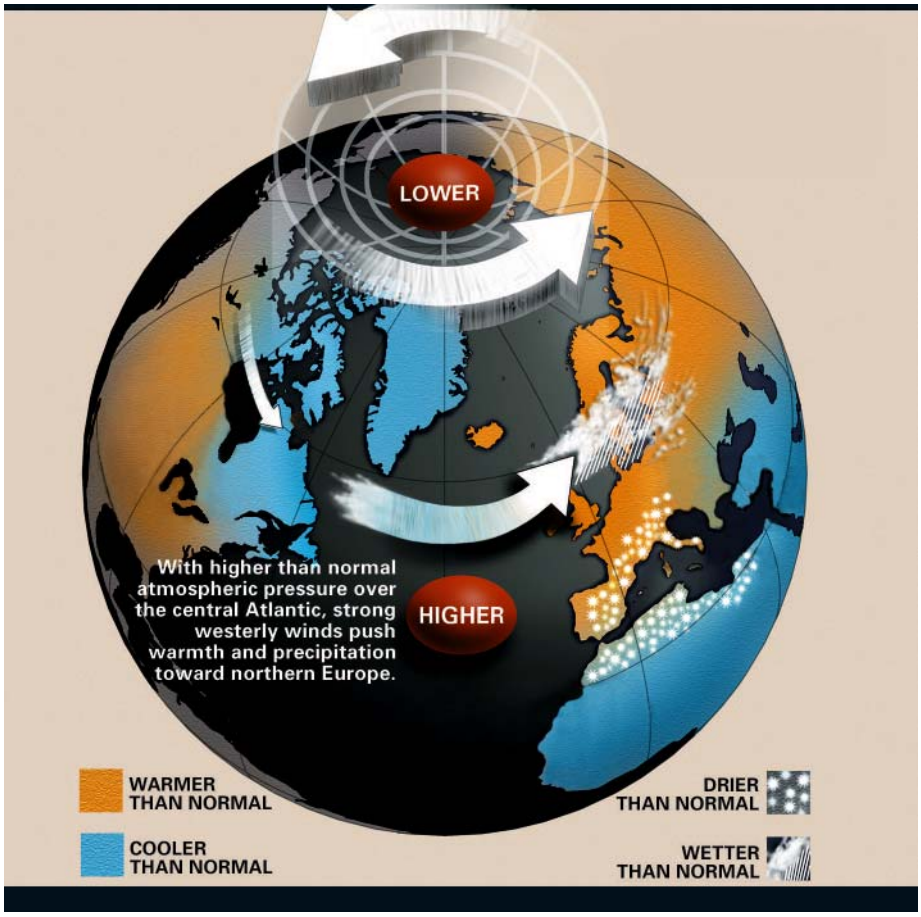

Box 3.1, Figure 1. Shown is a schematic of the changes associated with positive phase of the NAO and NAM. The changes in pressure and winds are shown, along with precipitation changes, and with warm colours indicating areas warmer than normal and blue indicating cooler than normal.

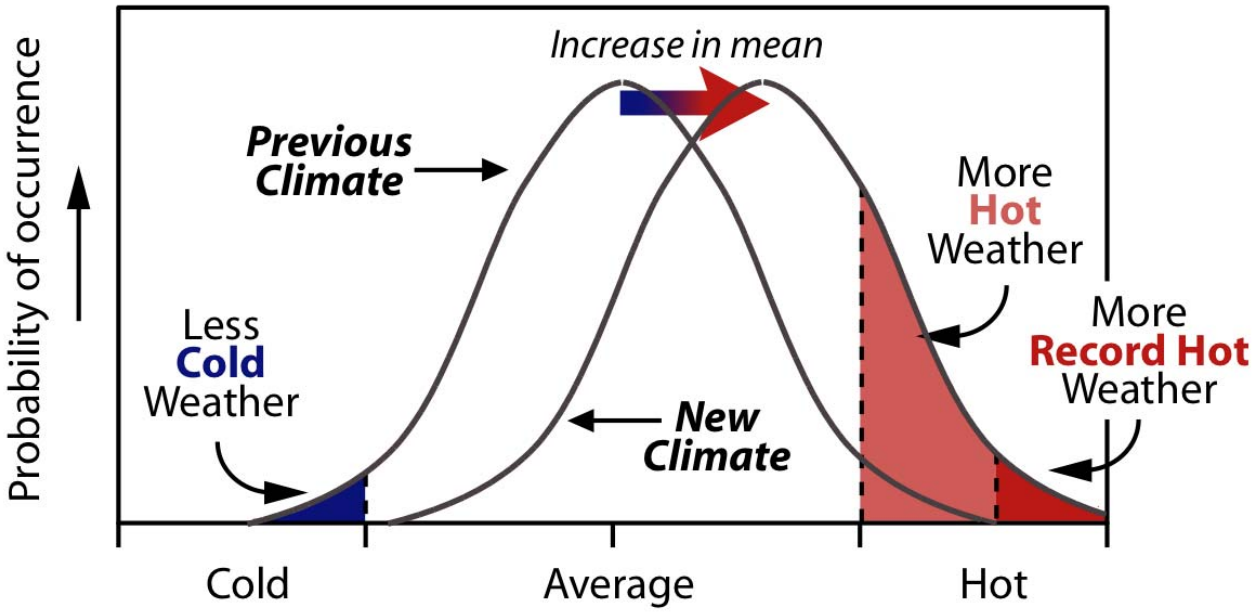

Box TS.3.4, Figure 1.

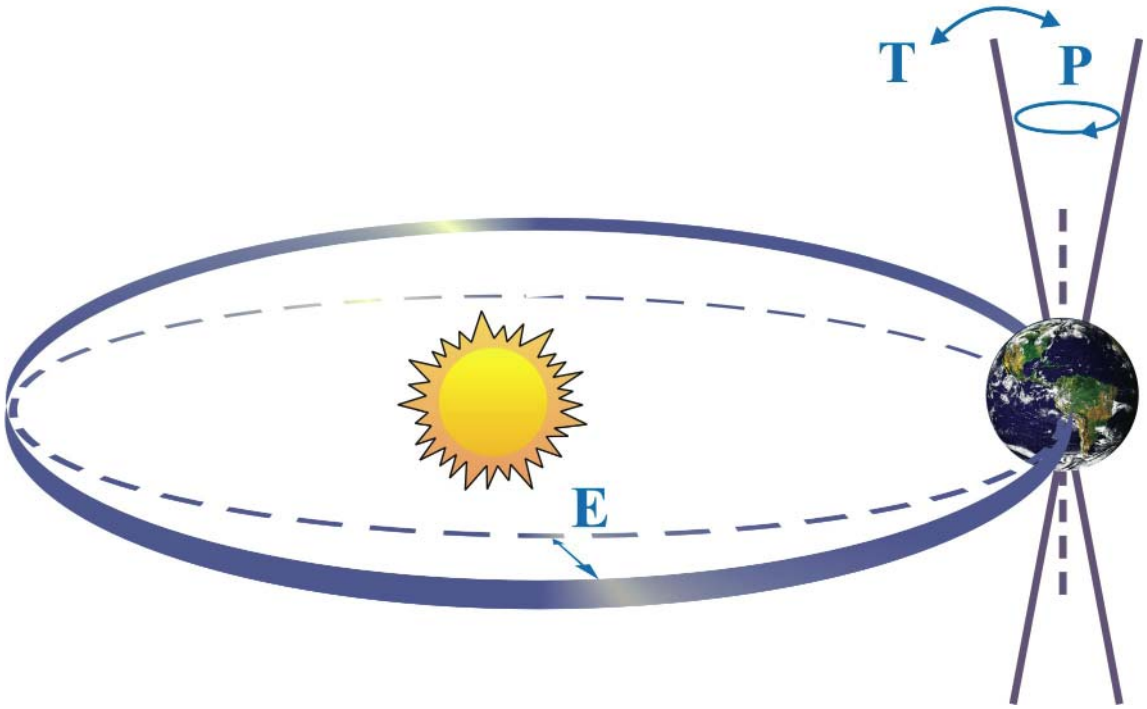

Box TS.3.5, Figure 1. Schematic of the Earth's orbital changes (Milankovich cycles) that drive the ice age cycles. "T" denotes changes in the tilt (or obliquity) of the Earth axis, "E" denotes changes in the eccentricity of the orbit, and "P" denotes precession, i.e., changes in the direction of the axis tilt at a given point of the orbit. {FAQ 6.1, Figure 1}